UNIVERSITA' DEGLI STUDI DI PADOVA

DIPARTIMENTO DI SCIENZE CHIMICHE

CORSO DI LAUREA MAGISTRALE IN SCIENZA DEI MATERIALI

TESI DI LAUREA MAGISTRALE

$La_{0.75}Sr_{0.25}Cr_{0.5}Mn_{0.5}O_3$ based anodes for Solid Oxide Fuel Cells

Relatore: Prof.ssa Glisenti Antonella

Controrelatore: Prof. Martucci Alessandro

LAUREANDO: Giraldin Arianna

ANNO ACCADEMICO 2018/2019

Index

Introduction

In recent years, the enhanced interest into environmentally friendly production of energy promoted researches aimed at decreasing pollutant emission and at increasing efficiency and renewability in energy conversion and storage. The objective is to avoid or minimize the use of fossil fuels.

Fuel cells have attracted attention because are highly efficient devices, that directly transform chemical energy of fuels into electrical energy, with low or no pollutants emission. In fact, combustion is not performed and dangerous pollutants such as NO_x and SO_x are not produced.

In this contribution, Solid Oxide Fuel Cells (SOFCs) are discussed and in particular a new efficient anodic material is proposed. The aim is to design, synthesize, characterise and optimize a possible alternative anode for fuel cells, analysing its properties and possible applicability. The state-of-the-art anodes for SOFCs, in fact, are not adequate to work for fuels different than hydrogen and at temperatures lower than 800-1000 °C; I consider very relevant the possibility of using C-containing fuels (also derived by wastes, or biogas, or natural gas) and the decrease of the operating temperature to intermediate values 600-750 °C could make the difference in terms of cost and durability of the device.

$La_{0.75}Sr_{0.25}Cr_{0.5}Mn_{0.5}O_{3-\delta}$ (*LSCM*) perovskite has been selected. This choice has been made analysing literature works on anode materials for Solid Oxide Fuel Cells (SOFCs) application. In next sections, Fuel Cells are described with particular attention on solid oxide ones. State of art anode is Ni-YSZ (Yttria Stabilized Zirconia) cermet. Its advantages and disadvantages are listed and discussed. After that, this work is focalised on *LSCM* synthesis and characterisation. The synthetic method utilised is the citric acid method also called *Marcilly* method. Different techniques have been used to characterise the powder of interest. In particular, XRD (X-Ray Diffraction) is used to understand the crystallographic structure, to evaluate the effective insertion of all constituents inside the perovskite crystalline cell and to carry out compatibility test with different electrolytes. TPR (Temperature Programmed Reduction) curves give information about the processes of reduction of the material of interest at different temperatures. XPS (X-Ray Photoelectron Spectroscopy) and EDX (Energy Dispersed X-Ray Analysis) give information about the species presented in the structure and

make possible the evaluation of eventual segregation processes. Moreover, the powder surface area is calculated using BET (Brunauer – Emmett – Teller Surface Area) method. Data concerning morphology and granulometry are determined using SEM (Scanned Electron Microscopy).

To test electrochemical performance of *LSCM*, a symmetric cell is prepared based on electrolyte supported geometry. At first, an accurate study on the electrode ink composition was carried out. Different inks have been elaborated to optimise the adhesion of the electrode on the electrolyte pellets surface. A composite ink made of *LSCM* powder and electrolyte material is found to be the better choice in terms of adhesion. The ink is deposited on electrode surface using the tape casting technique. The cell is electrochemically tested utilising EIS (Electrochemical Impedance Spectroscopy). Both hydrogen and methane have been used as fuel, and different working temperatures are selected.

Moreover, composite anodes made by impregnation method have been prepared. Nickel has been chosen to enhance *LSCM* proprieties. This new anodic material contains 5wt% of Ni and is characterised utilising the techniques mentioned above. Nickel possesses high catalytic activity but unfortunately suffers from C-deposition and poisoning when fuels different than hydrogen are used. In this work, I decide to circumvent this obstacle optimizing the amount of deposited nickel to avoid carbon deposition and other disadvantages connected to its utilisation. It has also to be considered that, unlike YSZ, perovskites are much more efficient in stabilizing nickel against sintering and the formation of Lanthanum based oxycarbonates helps in avoiding the problem of C-contamination. Impregnation method has been chosen to produce Ni@LSCM powder. So, the composite material is directly synthetized as a powder utilising *Marcilly method*. This procedure is a variation of impregnation optimized in our research group, that makes use of a complexing agent, citric acid, to favour the deposition of nickel in highly dispersed form. Symmetrical cells are prepared using tape casting method and are electrochemically tested using EIS and Z-Lab software was used for a detailed interpretation of data and thus to put into relation the electrochemical behaviour with the results of the characterization.

The content of each chapter is here reported:

- ***Chapter 1. Fuel cell technology overview.*** In the first chapter, fuel cells systems are described with particular attention on SOFCs. Anode material is the focus of this research and the state-of-the-art material limits are discussed.
- ***Chapter 2. Perovskite as an efficient anode material.*** Perovskite are tuneable materials; which proprieties can be easily improved. Starting from $LaCrO_3$, a material used as interconnect, *LSCM* is produced by a controlled doping.
- ***Chapter 3. LSCM synthesis and characterisation.*** *LSCM* synthesis and characterisation are reported in this chapter.
- ***Chapter 4. Cell study of LSCM.*** *LSCM* is used as electrode deposited by tape casting over an electrolyte pellet. Electrochemical Impedance Spectroscopy leads to analyse its electrochemical behaviour. Different ink compositions and electron collector materials have been tested. Measurements have been performed utilising both hydrogen and methane as fuel.
- ***Chapter 5. LSCM composite: Ni@LSCM.*** Nickel impregnation on *LSCM* is the content of this chapter. Ni@LSCM powder is characterised and collected data are then confronted with the ones of *LSCM.*
- ***Chapter 6. Cell study of Ni@LSCM***. Ni@LSCM sample is deposited by tape casting on YSZ pellets and tested with both hydrogen and methane as fuel. Electrochemical data are confronted with the ones of *LSCM* sample.

1. *Fuel cell technology overview*

Fuel cells are electrochemical devices that convert directly chemical energy into electrical energy.[1] The first fuel cell was fabricated in 1839 by William Grove. An advantage of these systems is the possibility to generate power with high efficiency. In fact, they are not controlled by thermodynamic limitations, as conventional heat engines. Moreover, there is not combustion and minimal amount of pollutant is generated. This makes them a source of clean energy.[1]

The fuel cell is made by three components: unit cell, stacks and balance of plant. The unit cell is the section where reactions occur. Single cells can be electrically connected in series, forming stacks to have the desired output voltage. Interconnect layer permits physical separation of single cells and their electrical connection.[1] Balance of plant provides feed stream conditioning, thermal and water management and electric power conditioning equipement.[1]

For material scientist, the most interesting part of a fuel cell is the unit cell. This is composed by an electrolyte sandwiched between two electrodes: anode and cathode. Schematically, the working principle of a fuel cell is represented in *Figure 1*.[1]

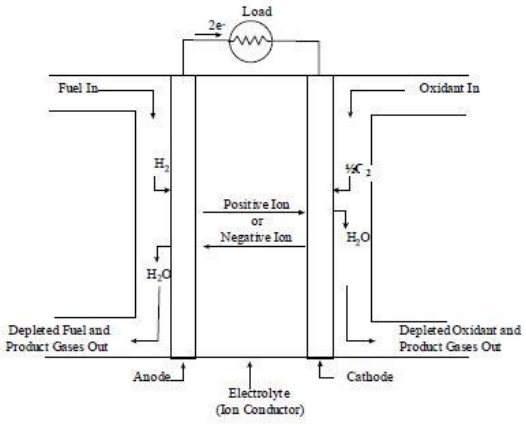

Figure 1. Schematic view of an Individual fuel cell.

Fuel, usually hydrogen or hydrocarbons, is fed to anode, the negative electrode. The use of hydrogen has some disadvantages connected with the high purity needed in low temperature fuel cells, the production, transportation and storage. To use hydrocarbons directly, it is necessary a cell that can work at high temperatures, in order to avoid the use of noble metals as electrocatalysts. An oxidant, usually oxygen, is fed to cathode,

the positive electrode. On the porous electrodes surface, electrochemical reactions of oxidation and reduction take place respectively on anode and cathode. Electric current flows through an external circuit. The electrolyte layer is inserted between electrodes, it is an ionic conductor and permits ions migration, closing the circuit.

Fuel cells are classified distinguish between different electrolyte materials, fuel, and working temperature. The principal types in relation to inlet and outlet gasses, temperatures and ions movement are listed in *Figure 2.* [2]

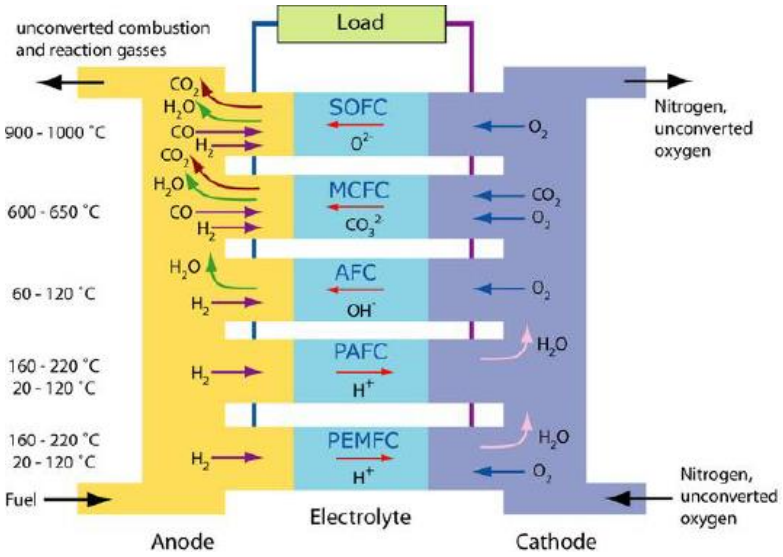

Figure 2. Schematisation of different types of fuel cells.

Fuel cells that work at temperatures between 20-200°C are called low temperature fuel cells. Instead the ones that work at higher temperature between 600-1000°C are intermediate-high temperature devices.

Proton Exchange Membrane Fuel Cells (PEMFC)

These cells work at temperatures between 30-100°C. The electrolyte utilised is a solid polymer. In this case, protons are mobile and can migrate inside the electrolyte from anode to cathode.[2] The key part of the cell is MEA (Membrane Electrode Assembly) that consists on an anodic, a polymeric and a cathodic layer.

The reactions that take place inside this device are:

Anode: $H_2 \rightarrow 2H^+ + 2e^-$

Cathode: $\frac{1}{2}O_2 + 2H^+ + 2e^- \rightarrow H_2O$

Low temperature is needed to maintain the membrane hydrated and guarantees the movement of H^+ ions inside the polymeric layer. This is an advantage because PEMFC can start to work quickly. Also, not corrosive fuel is utilised, and MEA can be sufficiently thin that compact cells can be made. The problem is that hydrogen oxidation and oxygen reduction necessitate of a catalyst active at low working temperature. So, platinum must be chosen as catalyst. Pure hydrogen must be feed at anode side reducing fuel flexibility. Another consequence to platinum presence is an enhanced cost. Also, water management to maintain the polymeric membrane hydrated has to be taken in account during system development. It is possible utilise this type of devices in automobile, in portable and stationary applications.[3] They can reach the 60% in electrical energy conversion with a reduction of 90% pollutants.[3]

Direct Methanol Fuel Cells (DMFC)

Direct Methanol Fuel Cells are built using the same materials in electrodes and electrolyte layers as in PEMFC. In this case, liquid methanol is directly supplied to the anode side.

The reactions involved are:

Anode: $CH_3OH + H_2O \rightarrow CO_2 + 6H^+ + 6e^-$

Cathode: $\frac{3}{2}O_2 + 6H^+ + 6e^- \rightarrow 3H_2O$

Methanol has the advantage to be a cheaper fuel than hydrogen, simply available and manageable but it does not possess a high-power density. These cells have low powers but higher theoretical specific energy density than lithium batteries.[4] This makes them useful in various applications as in portable electronics.[4] A drawback is methanol crossover that severely reduces the cell voltage, fuel utilisation and cell performance.[4]

Alkaline Fuel Cells (AFC)

These cells are utilised at low temperature like PEM. While the specie transported in electrolyte layer is OH^- ions. The electrolyte layer is an alkaline solution usually composed by sodium hydroxide (NaOH) or potassium hydroxide (KOH).

The reactions that take place inside this device are:

Anode: $H_2 + 2OH^- \rightarrow 2H_2O + 2e^-$

Cathode: $\frac{1}{2}O_2 + H_2O + 2e^- \rightarrow 2OH^-$

The advantages of this system are: low working temperature that makes them easy to handle and higher reaction kinetics than in acidic conditions resulting in a higher cell voltage and efficiency. The slow reaction rate is overcome using highly porous electrodes and platinum as catalyst.[2] A problem of cost is due to the presence of platinum but a lower amount of catalyst is needed than in PEM, thanks to the higher working temperature.[5] One of the main drawbacks is that the electrolyte is a corrosive liquid. Moreover, the KOH solution is sensible to CO_2 making necessary the utilisation of pure hydrogen and oxygen.[5]

Phosphoric Acid Fuel Cells (PAFC)

In this case, porous electrodes composed by platinum particles dispersed on carbon black are utilised. A liquid electrolyte made of phosphoric acid at 100% is chosen to make possible protons movement from anode to cathode.[6]

The electrochemical reactions involved are:

Anode: $H_2 \rightarrow 2H^+ + 2e^-$

Cathode: $\frac{1}{2}O_2 + 2H^+ + 2e^- \rightarrow H_2O$

Higher temperatures than in PEM enhance the reaction rate, decrease the necessity of extremely pure hydrogen as fuel and the quantity of platinum into electrodes.[6] The major disadvantage is the use of a corrosive liquid as electrolyte.

Molten Carbonate Fuel Cells (MCFC)

This type of fuel cells works above 650°C. Carbon dioxide and oxygen are fed to cathode. In this way, CO_3^{2-} ions are transported through the electrolyte material to anode in which hydrogen oxidation takes place.

The reactions involved are:

Anode: $2H_2 + 2CO_3^{2-} \rightarrow 2H_2O + 2CO_2 + 4e^-$

Cathode: $O_2 + 2CO_2 + 4e^- \rightarrow 2CO_3^{2-}$

The electrolyte material is made of a molten mixture of alkali metal carbonates, usually a eutectic mixture of lithium and potassium carbonates (62wt% Li and 38wt% K), that

at high temperatures forms a highly conductive molten salt. This temperature permits the utilisation of inexpensive catalysts. At anode side, nickel is selected and at cathode side, nickel oxide is preferred. Moreover, at anode not only hydrogen but also hydrocarbons can be used directly thanks to the favourable working temperature.[2]

1.1 Solid Oxide Fuel Cells

Solid Oxide Fuel Cells (SOFC) are solid-state devices. They use as electrolyte a solid, non-porous metal oxide that has ionic conductivity.[2] At cathode, oxygen is fed and it is reduced to O^{2-}. The oxide ions are transferred to the anode through the electrolyte. Hydrogen or hydrocarbons are fuel gasses at anode. They react with oxide ions leading to the production of water or carbon dioxide and electrons that are injected into the external circuit. This type of cell works at high temperatures between 800-1000°C. A schematic view of the system is here reported, see *Figure 3*.[2]

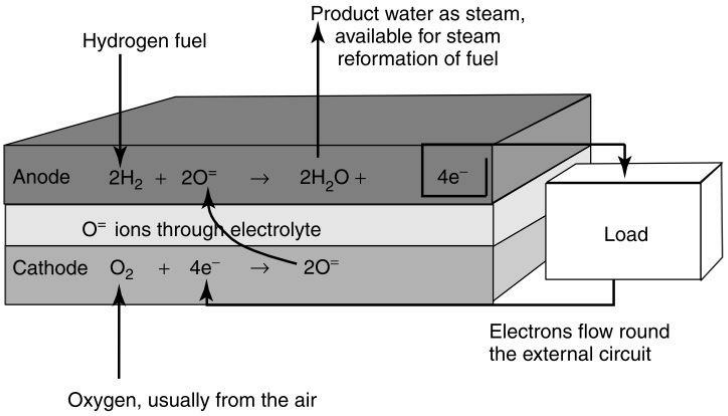

Figure 3. Schematic view of operating SOFC.

If hydrogen is used as fuel, the main reactions are:

Anode:

$$2H_2 + 2O^{2-} \rightarrow 2H_2O + 4e^-$$

Cathode:

$$O_2 + 4e^- \rightarrow 2O^{2-}$$

At electrolyte there is the movement of oxide ions from cathode to anode.[7]

The state-of-the-art materials used in each part of the cell and their characteristic are here reported:

Electrolyte.

The electrolyte must be an ionic conductor, and sufficiently dense to avoid the mixing of gases feed at anode and cathode. Moreover, it has not to be an electron conductor to avoid short-circuit. It must be chemical stable and possess mechanical strength especially in electrolyte-supported cells. Yttrium stabilised zirconia (YSZ) is usually utilised as electrolyte material. It has an appropriate ionic conductivity of O^{2-} species only above 800°C.[1] Other solid oxides electrolytes are: CGO (gadolinium doped ceria) and LSGM ($La_{0.9}Sr_{0.1}Ga_{0.8}Mn_{0.2}O_{3-\delta}$). Using these types of electrolytes, the operating temperature can be reduced until 600°C.

Anode.

The anode must be electronically conductive at high temperature and catalytic active for the oxidation of the fuel. Ni-YSZ cermet is the state of art material. It guarantees a good electronic conductivity and catalytic activity in relation to oxidation of hydrogen and hydrocarbons. Its advantages and drawbacks are deeply discussed in next sections. In this work, a new anodic perovskite-based material is proposed. Its characteristics are discussed in next sections.

Cathode.

The cathodic material must be electronically conductive at high temperature and catalytic active for oxygen reduction.[8] Sr-doped $LaMnO_3$ (LSM) is usually utilised as cathode. It is a p-type perovskite that exhibits mixed ionic and electronic conductivity.[2]

In SOFCs, a critical part is the so called Three-Phase Boundary interface (TPB). In these regions, there is the contact between fuel, usually a gas, electrode, with electronic conductivity, and electrolyte that possess ionic conductivity. These three phases interact in a specific region to make cell working. In fact, electrochemical reactions take place in a region electrocatalytic active, in contact with electronic conductive electrode and with the electrolyte that supplies oxide ions. To enhance TPB, the electrode is preferably a MIEC (Mixed Ionic and Electronic Conductor). In this way the cell power and efficiency are improved. Also, the region where the electrocatalytic reactions occurs is bigger. This depends on the fact that all the surface of the

anode/cathode can transfer/collect electrons to/from the external circuit and it can collect/transfer oxide ions from/to the electrolyte. In *Figure 4*, it is possible to see the enhancement of the active area thanks to the utilisation of a MIEC anode.[2]

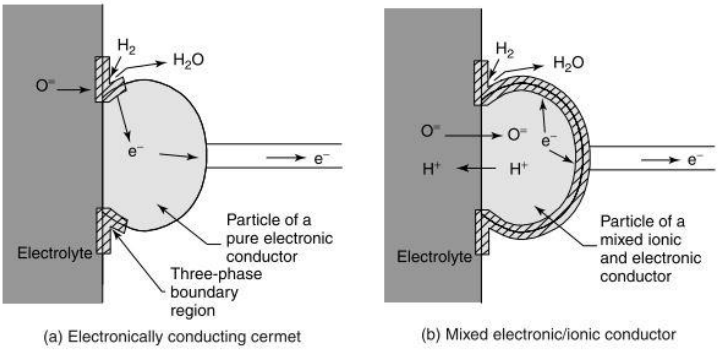

Figure 4. Three-phase boundary regions of different anodic materials. In (a) electrode possess only electronic conductivity, instead in (b) it is a mixed ionic and electronic conductor

SOFCs work at elevated temperature because of the presence of a solid-state electrolyte material. In fact, the ionic conductivity of YSZ electrolyte is activated only above 800°C. The use of different electrolytes materials, such as LSGM reduces the working temperature.[9] In this case it is possible to have devices that work efficiently at 600°C. High working temperatures are connected with numerous advantages and disadvantages: chemical and mechanical stability at the operating conditions and absence of reactions at the interfaces, as an example, are fundamental requirements.[10] Also, the thermal expansion coefficient of cell constituents has to match, to avoid delamination. To achieve high working temperature higher start-up time is needed and the cost for thermal management is increased. In contrast, there is a higher flexibility in fuel selection: high working temperature makes possible the use of fuel that differs from hydrogen. In particular, it is possible to direct inlet hydrocarbons at anode side without an external reformer system.[9] Selected materials are usually cheaper than the ones needed in other types of fuel cells.[10] Low temperature fuel cells utilise noble metals like platinum to assure catalytic activity and conductivity, the high temperature avoid this requirement. These devices can produce electricity with negligible amount of pollution, they are environment-friendly with a theoretical efficiency of 60%.[11] So, a highly power conversion is achieved. They can produce energy for small-medium scale stationary applications but they have an elevated management cost due to high working temperature.[11]

1.2 SOFC thermodynamics

The value of open circuit voltage (E°) of a hydrogen fuel cell is thermodynamically determined by this formula: $E° = -\Delta G_f/2F$. The theoretical value of OCV obtained at 100°C is of 1.2V. The real cell voltage is always lower than the theoretical one. The useful voltage output, V, under load conditions is equal to:

$$V=E°-IR-\eta_a-\eta_c$$

where I is the current, R the electrical resistance of the cell and η_a and η_c the polarisation resistance of anode and cathode respectively.[12] The correlation between voltage and current density is reported in the figure below (*Figure 5*). It is possible to note that the shape of the real curve is different from an ideal 'no loss' value.[2] The initial fall in voltage is small, the open circuit voltage is close to the theoretical one. The graph is then fairly linear since a voltage fall at high currents.

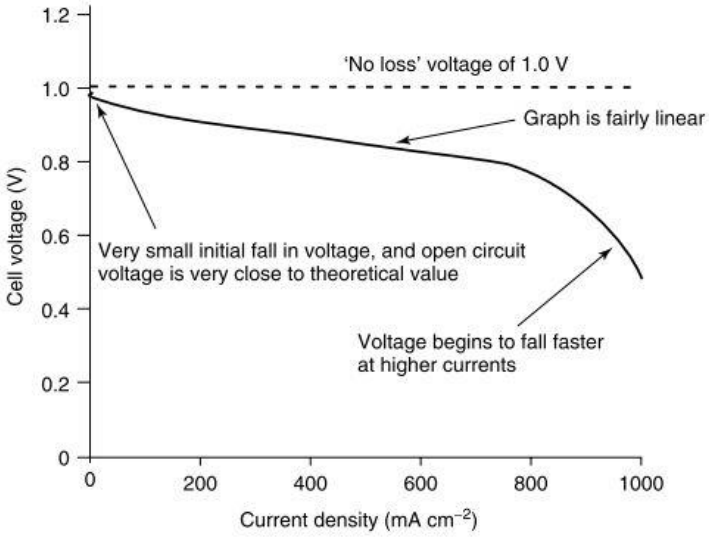

Figure 5. Graph showing the voltage of a typical air pressure fuel cell operating at about 800°C.

The voltage loss is due to different parameters. The ohmic loss element is due to electrolyte and electrodes internal resistance. To reduce this term, it is preferred fabricate dense, thin and gas-tight electrolyte ceramic membrane.[13] In addition the electrode/electrolyte interfaces can take an important role.

The electrical resistance of electrodes is related to their internal resistance, contact resistance, concentration polarization resistance and activation polarisation resistance. The prevalent loss mechanism depends on the current density level. The internal ohmic

resistant is due to the transport of electrons through anode and consequently to its resistivity and thickens. It is directly proportional to cell resistance.[12] Contact resistance refers to poor adherence between anode and electrolyte layers. Concentration polarisation is caused by the transport of gaseous species inside anode. It is prevalent at high current density because becomes difficult have enough reactant flow at reactive sites. It depends on the porosity, microstructure and pore size of electrode. Activation polarisation is due to charge transport process at TPB and the slowness of reactions taking place on the surface of electrodes.[13]

1.3 Anode material

At anode electrode, the reaction that takes place is oxidisation of the fuel. The material chosen has to be catalytic active, high ionic and electronic conductive (>100 S cm^{-1}) to reduce problems connected to the three-phase boundary area. To enhance oxygen diffusion coefficient significant amounts of anion vacancies are required and also anion lattice disorder can be of some help.[14] Moreover, it has to be chemically compatible with the other components of the cell and thermally stable at working temperature.[7] A porous structure with catalytic particles widely dispersed is needed to give the possibility to the gas to be in contact with a higher active area. Another useful characteristic of anode material is high wettability with respect to electrolyte substrate and the presence of continuous channels to allow rapid transport of gas.[13] It has also to be resistant to sulphur, carbon formation and to other impurities present in injected gases. Low cost materials and fabrication are needed to enhance its possible commercialisation.[13]

Hydrogen is a clean fuel and usually preferred in fuel cell technology. It is necessary high cost of production, infrastructure setup, efficient methods of carrying and storage. [14] Nearly 75% of hydrogen is derived from steam reforming of natural gas in large scale plants.[15] To avoid these problems, other fuels have to be reactive into fuel cell environment. Especially SOFC technology can permit the utilisation of hydrocarbons as fuel, thanks to the high working temperature.

1.3.1 Reactions using hydrocarbons as fuel

In *external reforming*, the raw fuel is converted into a hydrogen-rich gas in an external reactor, before the introduction into the cell. Most of the external reformers favour the steam reforming reaction that gives the highest amount of hydrogen and efficiency.

Steam reforming reaction: $CH_4 + H_2O \leftrightarrow CO + 3H_2$

In this case hydrocarbons are inlet into the reformer with a certain amount of water. Steam reforming is a highly endothermic reaction ($\Delta H° = 206$ kJ/mol) and takes place at temperatures above 500°C.[16] This process can be performed through *indirect internal reforming* and *direct internal reforming*. It is generally associated to gas shift reaction.

Gas shift reaction: $CO + H_2O \leftrightarrow CO_2 + H_2$

The *external reforming* needs heat-exchange arrangements that decrease efficiency and enhance costs. The advantage of this system is the flexibility of fuel processor design independently of the fuel cell stack. Deactivation of the anode material caused by carbon formation is less favoured.[17]

The *internal reforming* can be applied thanks to the high working temperatures and the presence of a catalytic active anode material.

In the case of *indirect internal reforming*, a reforming layer is directly introduced into the stack by coating the hardware parts of the anode chamber. This approach leads to better heat-transfer efficiency and low cost compared with external reforming, but the reactions control is more difficult.[17]

Direct internal reforming leads to the highest efficiency and less cost. In this case, the reforming takes place on anode surface along with oxidation of hydrogen and carbon monoxide. Internal reforming by total or partial oxidation implies the total conversion of hydrocarbons to hydrogen. These reactions can be schematised in this way:[9]

$$CH_4 + H_2O \rightarrow CO + 3H_2$$
$$CH_4 + 2H_2O \rightarrow CO_2 + 4H_2$$

Followed by electrochemical reactions like:

$$H_2 + O^{2-} \rightarrow H_2O + 2e^-$$

$$CO + O^{2-} \rightarrow CO_2 + 2e^-$$

Water produced by the electrochemical reaction above favours water gas shift (WGS) that minimises carbon deposition through carbon gasification reaction. The last-mentioned reactions are schematised below:

Water gas shift reaction: $H_2O + CO \leftrightarrow CO_2 + H_2$

Carbon gasification reaction: $H_2O + C \leftrightarrow CO + H_2$

Direct internal reforming reactions lead to a lower need of thermal management of the cell and increase efficiency avoiding the energy penalty connected with heat transport from external reforming. In fact, electrochemical oxidation and high cell temperature facilitate endothermic reforming reactions. While there are several drawbacks in relation to materials failure, carbon formation, decrease in cell performance and durability.[17]

Direct electrochemical complete oxidation can be schematised in this way.[9]

$$CH_4 + 4O^{2-} \rightarrow CO_2 + 2H_2O + 8e^-$$

In this case the fuel is directly supplied to the anode side and the electrochemical reactions take place without the formation of hydrogen. CO_2 and H_2O produced electrochemically reform the incoming fuel into syngas that can be further electro-oxidised. Expensive reforming systems are avoided but there are several disadvantages connected with coke formation. It is also possible that *partial oxidation* is performed instead of complete oxidation:

$$CH_4 + 3O^{2-} \rightarrow CO + 2H_2O + 6e^-$$

It yields fewer electrons per mole of fuel.[18] These reactions are performed in electrocatalytic active part of electrode and involve the transfer of charged species. Reactions like steam/dry reforming and cracking occurs in inactive regions, so they can be called non-charged transfer reactions.

In the scheme below, *Figure 6*, different types of reforming reactions are compared.

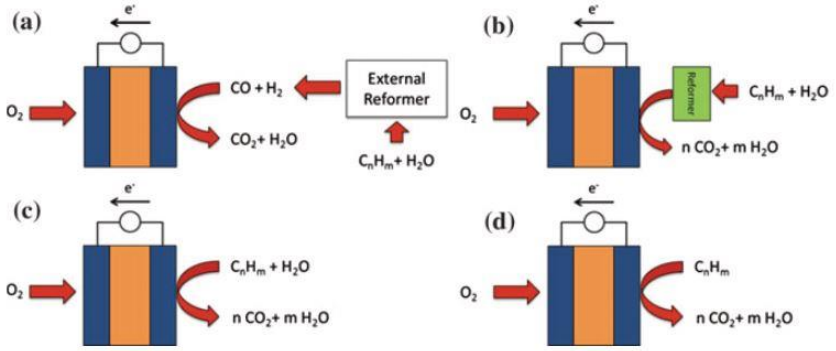

Figure 6. Fuel processing modes. (a) External reforming. (b) Indirect internal reforming. (c) Direct internal reforming. (d) Direct fuel oxidation.

1.3.2 State of art: Ni-YSZ

The state-of-the-art anode is a cermet made by Ni and YSZ. It is the most used material because of its low cost and its high stability in reducing atmosphere.[13] The utilisation of a cermet gives numerous advantages. In a single material it is possible to achieve an adequate electronic conductivity, electrocatalysis and microstructure.[10] The mixture of Ni particles with YSZ gives an higher matching with the thermal expansion coefficient of the electrolyte. Ni provides catalytic activity and electronic conduction.[8] It is a steam reforming catalyst that promotes the C-H bond rupture, and an electrocatalyst for electrochemical oxidation of hydrogen.[13] YSZ gives high ionic conductivity and also separates Ni nanoparticles avoiding agglomeration.[10] The composition of Ni-YSZ usually contains a 40-60% of Ni. To have the adequate porosity, NiO powder is mixed to YSZ and reduced to Ni. It has good mechanical proprieties also for the utilisation of anode-supported structures.[1] Moreover, it has low cost and the production is less expensive than the one of other anodes that has been proposed.[19]

The drawbacks of this anodic material are various:

- Ni-YSZ produced by reduction of NiO is instable in air. If Ni-YSZ is exposed to air, Ni can be re-oxidised to NiO especially at elevated temperatures.[20] The continuous oxidation/reduction processes produced large volume change.[1] Consequently, it can determine the degradation of the cell and the reduction of its performance.[10]

- It has poor activity in direct oxidation of hydrocarbons, injected as fuel. The formation of carbon is preferred, and consequently the porosity of the electrode is reduced.[1] The cooking of Ni-YSZ anode leads to performance degradation.[21] In this way, Ni sites are covered by carbon that is not active for the electrochemical reactions.[21]
- Ni-YSZ is sensible to contaminants. In particular, it is poisoned by H_2S. This fact prevents the utilisation of this anode material in the case that natural gases are used as fuel.[22]
- The thermal expansion coefficient is higher than the one of usually used electrolytes and cathodes. This implies that long time mechanical stability is not sufficient.[1]
- It can react with some La containing electrolytes.[10]

As previously said, the internal reforming can enhance the performance and reduce the cost. The major problem is that utilising Ni-YSZ as anode material methane cracking is favoured. Methane cracking reaction can be schematised as:

$$CH_4 \rightarrow C + 2H_2$$

To avoid it, a large quantity of steam has to be mixed with methane.[23] The methane cracking reaction is detrimental for the anode material because a huge quantity of carbon is deposited, with a consequent lowering of electrode performance. Moreover, the high velocity of steam reforming reduces the quantity of methane that can directly react. The methane is locally reduced near the injection system and this cause a cooling down effect because the steam reforming is an endothermic reaction.[23]

It is necessary to find a new anode material that can catalyse steam reforming not too fast, inert to methane cracking, good electrocatalyst for hydrogen electrochemical oxidation, and compatible with SOFC operative conditions.[23]

1.4 Reversible fuel cells (Re-SOC)

Electrical energy storage (EES) is an actual challenge for future electric grid. The possibility of temporal decoupling electric power generation and consumption has led to find a technology capable to overcome this necessity. To achieve the requirement of optimised EES, the possibility of using reversible solid oxide cells (ReSOCs) has become much more important. ReSOCs are devices that work in both fuel cell and electrolyser modality. The ReSOCs' stack can be schematised as depicted in *Figure 7*.[24]

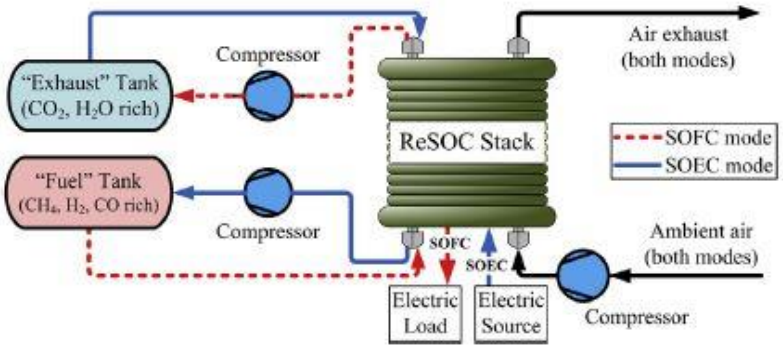

Figure 7. Simplified schematic of a stand-alone energy storage system utilising reversible solid oxide cells (ReSOCs).

ReSOC is a solid-state electrochemical energy conversion device that can operate at high temperature. This technology works with high efficiency (>70% roundtrip) and as a cost-effective energy storage device at large-scale (>4US¢/kWh/cycle).[24] It is composed by the state of art material for solid oxide fuel cell applications. Moreover, it has to be capable to work also in electrolyser modality. As fuel cell, it can consume fuel and produce energy. If it works like an electrolyser, it uses electrical energy and reactant species as H_2O and CO_2 to produce fuel. These two modalities can operate alternative in a single device, depending on energy necessity. The reactant produced in fuel cell/electrolyser modality are then compressed and stored to overcome operator necessity. So, a device formed by electrode materials that can operate both as cathode and anode efficiently and stable at different atmospheres is needed.

One significant challenge is thermal management. SOFC modality requires excess heat rejection while SOEC mode needs heat supply to maintain desired working temperature. It is important to find adequate conditions (T,p) that can permit elevate performance in both operation modalities. It is necessary to integrate different temperatures that characterise the gas storage and the operative cell. In addition,

storage of gas has to be performed via minimal energy needed pressurisation. Also, overcoming the endothermic electrolysis process to make the system thermally self-sustaining is an important issue.[24]

Working at both operating methods permits a lower degradation of the cell system. Reversible cycling cell is more stable and in particular the carbon formation is reduced. In this way, hydrocarbon fuels can be used without detrimental effects on the system.

1.5 Symmetrical fuel cells (S-SOFC)

A new concept of fuel cells can be studied: in these fuel cells the same material can be used as anode and cathode simultaneously. This type of cells is called symmetrical fuel cells (S-SOFCs). They are intrinsically reversible devices. The symmetrical configuration permits the reduction of the number of elements from three to two facilitating the assembly in a single thermal treatment, minimising interdiffusion between cell components and thermal expansion coefficient compatibility. Moreover, sulphur poisoning and carbon deposition can be reduced because the reversing of gas flow can oxidise any sulphur species and carbon deposit.[25] The required material should have good capability working as anode and as cathode material. It should have catalytic activity towards oxygen reduction and fuel oxidation, chemical stability and good mixed ionic and electronic conductivity in both atmospheres.

2. *Perovskites as an efficient anode material*

Oxide anode has been identified like a good alternative to the state of art material, Ni-YSZ. Most of the perovskite based oxide materials are immune to carbon deposition, mixed ionic and electronic conductors and possess catalytic activity.[14] In particular, the perovskite family has attracted interest because of the wide choice of possible cations that can form stable structures. In fact, the 90% of the metallic natural elements of the Periodic Table are stable as perovskite.[26] Moreover, doping on A or B-site produces a structure of $A_{1-x}A'_xB_{1-x}B'_xO_3$ type. Multicomponent perovskites can have enhanced catalytic and conductive proprieties and achieve the performance required. Some perovskite can accommodate a large amount of oxygen vacancies making them ionic conductors.[14]

2.1 Perovskite structure

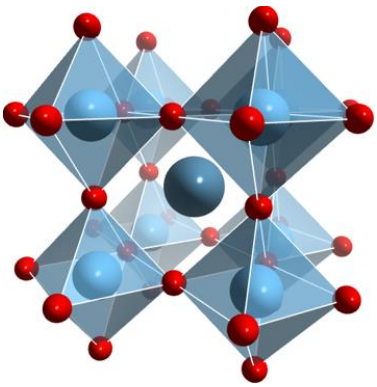

Figure 8. Perovskite structure.

The perovskite structure was first described by a geologist, Gustav Rose in 1830. He was studying $CaTiO_3$, the archetypal perovskite. This sample was named in honour of the Russian mineralogist Count Lev Aleksevich von Perovski.[27]

The general formula of perovskite-type oxide is ABO_3 and it can be represented as in *Figure 8*.[27] A-site cations have a large ionic radio and a coordination to oxygen atom of 12. B-site cations have a smaller radius and a coordination of 6 in relation to oxide ions. A-cations and O-anions create a cubic closest packing and B-cations occupy the octahedral sites. It is described by *Pm3m-*O_h space group.[26]

To form a stable perovskite, the radius of A, r_a, B, r_b, and O, r_o, have to satisfy the Goldschmidt relation:

$$0.8 \leq t = \frac{r_a + r_o}{\sqrt{2}(r_b + r_o)} \leq 1$$

with *t*, the tolerance factor. This rule is applicable at room temperature to the empirical ionic radii. The tolerance factor gives information about the deviation from ideal structure. If *t*=1 the ideal structure is achieved, in which atoms are touching one

another.[26] It is possible the presence of deviations from ideal structure with orthorhombic, rhombohedral, tetragonal, monoclinic and triclinic symmetries. These may exist at room temperature while at elevated temperature the cubic structure is always stable.

Another condition that has to be satisfied is the electroneutrality. The total charge of O-anions has to be equal to the sum of the charges of A and B-cations. Partial substitution in A and B can be achieved but conserving electroneutrality. Moreover, there is the possibility of O-site deficient structures. This leads to the creation of new defective materials with interesting proprieties.[26]

A-site is generally occupied by rare-earth and/or lanthanoid cations. B-site elements are transition metals of the first row of Periodic Table. Varying oxygen partial pressure they change oxidation state, giving electronic conductivity to the material. B-site cations can increase thermal stability, controllable valence, vacancies production and catalytic activity. The use of two different ions in B-site can give synergistic effects. In fact, the combination of cations proprieties and creation of new ones can enhance the catalytic and conductive ability.[27]

The concentration of oxygen vacancies is a function of the oxidation states of A-site and B-site cations. If the sum of total charges on A and B sites is 6+ and balanced the charge of oxide ions, there is not presence of oxygen vacancies. It is most likely that oxygen vacancies are formed if B-site cations are reduced.[28]

Thanks to their capability as electronic and ionic conductors, perovskite materials have attracted interest for the application as electrode materials. There are several advantages using them as anode material. The ionic conductivity can enhance the TPB region and the performance of the cells. Metal oxides are poor reforming catalyst and they avoid carbon fibres formation. They are resistant to sintering and can maintain anode porosity under low oxygen pressure conditions. Moreover, the possibility of being catalytic active in relation to hydrocarbon oxidation has enhanced their studies as anodic functional material [8]

2.2 Interconnect material

Multiple cells are stacked together to enhance the voltage output. To connect them in series, interconnect material is needed. Interconnect physically separates and electrically connects anode of one cell to cathode of the next one. The interconnect has to possess several qualities and it is one of the most demanding part of a fuel cell.[12] Following characteristics have to be fulfil:

- It must have electrical conductivity in the operating conditions of SOFC.
- It has to be stable in terms of dimension, microstructure, chemistry and phase at operating temperature in reducing and oxidising atmosphere. If there is any dimensional change, it can lead to the rupture of the cell. The microstructure of interconnect should be immune to chemical potential gradients to avoid variation in electrical conductivity during utilisation.
- To avoid the combination of oxygen and hydrogen it has not to be permeable to gasses.
- Thermal expansion coefficient (TEC) has to be comparable to the one of electrodes and electrolyte at ambient and operating temperature.
- Chemical stability and no reactivity with other cell components are needed.
- Good thermal conductivity is required. It guarantees that heat generated by exothermic reactions on cathode side can be transported to anode where endothermic reactions take place.
- It has to be resistant to oxidation, sulfidation and carburisation.
- Easy fabrication and low-cost materials are preferred to facilitate the exploitation of the product to commercialisation.
- Mechanical stability, high-temperature strength and creep resistance are required proprieties.

Various materials have been proposed as metallic alloys and perovskite materials.[12] Perovskite materials have demonstrated compatibility with the requirements of interconnect materials and with materials commonly used in SOFC. Even if they possess some drawbacks connected with rigidity and mechanical flexibility.[1]

2.2.1 State of art: $LaCrO_3$

$LaCrO_3$ has demonstrated adequate proprieties to be used as interconnect material. In fact, it possesses electronic conductivity and stability at elevated temperature and under both reducing and oxidising atmosphere.[10] Moreover, it has moderate stability in fuel cell environment and with other cell components in terms of phase, microstructure and thermal expansion.[12] It is a p-type conductor: negative charged cation vacancies can form and are electrically compensated by positively charged electron holes. Electrical conduction can be described by the small polaron mechanism, due to the transport of electron holes. The nonstoichiometric reaction that guarantees p-type conductivity is:

$$\frac{3}{2}O_2 \leftrightarrow V_{La}''' + V_{Cr}''' + 3O_x^x + 6h^{\cdot}$$

With V_{La}''' and V_{Cr}''' refers to La and Cr vacancies, O_x^x is oxygen site and $h^{\cdot}$ electron hole, using Kroger-Vink notation.

To improve electrical conductivity, the perovskite can be doped in A or B-sites creating a structure of the formula: $La_{1-x}M_xCr_{1-y}N_yO_3$. M usually refers to Sr or Ca species and N to Mn, Fe, Ni, Cu or Co. Under high oxygen activity environment ($p(O_2)=10^{-8}$ atm) the negatively charged M_{La}' and N_{Cr}' are electronically compensated by chromium oxidation: $Cr^{3+} \rightarrow Cr^{4+}$.[12] In the case of doped $LaCrO_3$, the electrical transport is dominated by small-polaron hopping of the localised charge at Cr-sites. The conductivity has a strong dependence on oxygen partial pressure, especially in low oxygen activity environment. In this condition, ionic compensation mechanism is dominant, thanks to the presence of oxygen vacancies.

The equilibrium at low oxygen activity can be described as:

$$\frac{1}{2}O_2 + V_{\ddot{O}} + 2Cr_{Cr}^x \leftrightarrow O_x^x + 2Cr_{\dot{C}r}$$

With Cr_{Cr}^x is Cr sites and $V_{\ddot{O}}$ is oxygen vacancy. At reducing conditions, there is the formation of oxygen vacancies to maintain electroneutrality. So, both ionic and electronic compensation mechanisms are present, and ionic is the dominant one. The electrical conductivity decreases at low oxygen pressure due to a reduction of electron

hole concentration. An increased doping enhances the electron hole concentration and electrical conductivity.[12]

Summarising, under oxidising environment as on cathode side ($10^{-0.7}$-10^{-4} atm), doped-$LaCrO_3$ exhibits electronic compensation mechanism with an induced transition between $Cr^{3+} \rightarrow Cr^{4+}$. However, at low oxygen pressure (10^{-8}-10^{-18}atm), as in anode side, the electrical conductivity is low because of the presence oxygen vacancies via ionic compensation mechanism. $LaCrO_3$ presents an internal gradient when it is utilised as interconnect, generating a loss in mechanical strength. The electrical conductivity is sufficient only at temperatures above 800°C. Below this temperature, it is exposed to degradation.[12]

2.3 $La_{0.75}Sr_{0.25}Cr_{0.5}Mn_{0.5}O_{3-\delta}$

$LaCrO_3$ has also been proposed as a potential anode material thanks to its proprieties, previously mentioned. However, performances of the pure perovskite are not sufficient. So, it has been proposed partial substitution of Cr and La.[10] Alkaline earth elements like Ca, Sr and Mg on A-site can be substituted in $LaCrO_3$ structure. On B-site, Cr can be replaced by a more reducible first-row transition metal like Mn, Fe, Co and Ni.[29] In this way, a stable, catalytic active and mixed conductor perovskite can be made.

Sr and Ca doped $LaCrO_3$ inhibits cooking and carbon formation if the substitution on A-site is present in low percentage (about 20%). These doping elements are not electrocatalytically active under pure methane feed, but their substitution can enhance oxygen ion vacancies number and consequently ionic conductivity. Thanks to TPR tests, it is evident that lattice oxygen is stabilised by Sr>Ca at A-site. On A-site, Ca and Sr improved the catalytic activity toward methane oxidation.

$LaCrO_3$ has not weight loss when exposed to a reducing atmosphere ($p(O_2) = 10^{-21}$atm at 1000°C). This indicates that chromium maintains six-fold coordination in Cr^{3+} oxidation state. In this case, oxygen vacancies and ionic conductivity are difficult to achieve without doping. In B-site, multivalence transition metals are selected as dopants because they can change their oxidation number and easily tolerate oxygen vacancies in a reducing atmosphere at high temperature.[30] To increase the catalytic activity, oxygen ion vacancies and electronic conductivity of stable doped chromite,

substitution on B-site has been performed. On B-site, lattice oxygen is easily removed by doping of Mn>Ni>Co. Co inhibits catalytic activity, instead Mn and Fe give an enhanced activity in contrast to undoped perovskite. Co and Mn have the lowest cracking activity in opposition to Fe that leads to the deposition of a higher amount of carbon. Ni in a low amount can enhance catalytic activity and methane oxidation avoiding methane cracking and carbon deposition.[29]

Tao et al. have proposed the partial substitution of Cr with Mn, forming $La_{0.75}Sr_{0.25}Cr_{0.5}Mn_{0.5}O_{3-\delta}$ (*LSCM*).[30] Usually on B-site, the dopant adding is up to 20%. In this case, two transition metals species occupy the B-site in excess of percolation limit (>33%).[30] Only if Mn is chosen as dopant ion, the perovskite is sufficiently stable at this elevated quantity of doping. The chemical stability of *LSCM* increases with an increased amount of Cr content. Instead, the electrical conductivity decreases with an enhanced Cr content and increases with the Mn content.[31] The thermal expansion coefficient is 9.3×10^{-6} K^{-1} in air, comparable to the one of YSZ, and 10.3×10^{-6} K^{-1} in both air and hydrogen. It also matches the thermal expansion coefficient of LSGM.[32] It is stable at elevated temperature in both oxidising and reducing atmosphere, and operating with methane.

Mn like Cr supports p-type conduction in oxidising conditions, Mn can also possess lower coordination numbers and it can enhance oxide-ion migration and conductivity.[30] These proprieties can make the perovskite a MIEC and catalytic active material. So, *LSCM* is a good candidate as anode material. As a p-type conductor, the operating couple Mn^{4+}/Mn^{3+} is completely reduced in hydrogen and methane atmosphere to Mn^{3+}. So, the electrical conductivity is lowered in reducing atmosphere.[33] It shows a p-type conductivity that decreases with decreasing $p(O_2)$, instead ionic conductivity increases due to the presence of oxide ion vacancies.[10] It has comparable performance to Ni-YSZ in hydrogen atmosphere.[30] The substitution of Sr on A-site leads to a charge compensation mechanism of Cr^{3+}/Mn^{3+} in Cr^{4+}/Mn^{4+} that results in an enhanced small polaron mechanism and consequently conductivity.

At low oxygen pressures the mechanism of oxygen vacancies formation can be described as:

$$2M_M + O_O^x \leftrightarrow 2M_M^x + V_{\ddot{O}} + \frac{1}{2}O_2$$

With M stands for Cr and/or Mn.[34]

The lattice expansion in reducing conditions related to reduction of B-site ions can enhance the M-O-M bond inhibiting the transport of polarons. This can decrease the electronic conductivity at low (pO_2).[34] However, an increase of oxygen vacancies can give an higher oxide-ionic conductivity.

In H_2 atmosphere, it is the oxygen loss that reduces the carrier concentration.[31] Under fuel cell operating conditions, a certain amount of oxygen ions passes through the electrolyte layer so the anode conductivity will be enhanced. The rate-limiting step is assumed to be the chemisorption reaction instead of the diffusion.[33] If the total formation of Mn^{3+} species is reached, the introduction of an electronic conductor is needed to achieve an adequate electrical conductivity. It has to be considered, however, that if H_2S is pumped with hydrogen at the anode ($10\%H_2S$-H_2), the formation of some impurities as MnS, La_2O_2S contaminations was observed.[31]

Methane oxidation is active at high temperatures in the absence of excess steam. Catalytic tests demonstrated that steam reforming is not the predominant reaction using methane as fuel. In fact, direct complete oxidation of methane is the most important reaction, even if steam is present. Complete direct oxidation leads to the direct utilisation of methane as fuel without an external reformer. The CO_2 selectivity is 100% at 800°C and below. If higher temperatures are utilised the selectivity for CO enhances, and partial oxidation became preferred.[35] At open circuit, when the oxygen stoichiometry is in equilibrium with the fuel gas, hydrocarbons cracking followed by electrocatalytic oxidation is favoured. An increased ionic flux through the electrolyte material leads to an increased nonequilibrium oxygen presence in *LSCM* lattice that can decrease polarisation resistance with increasing current density. An increase in current density makes total oxidation the most favoured reaction.[18]

The catalytic activity and selectivity over total oxidation decrease with decreasing of oxygen stoichiometry, 3-δ. At 700°C, with high oxygen stoichiometry (3-δ close to 3) the total oxidation is favoured, instead with lower oxygen stoichiometry (3-δ less than 3) partial oxidation is preferred. In the case of low oxygen content, two mechanisms can give the same type of response: partial oxidation (one step mechanism) and total oxidation followed by steam/dry reforming (two step mechanism). Partial oxidation is due to a higher amount of oxidised reaction sites, the fraction of surface reactions sites

decreases in low oxygen stoichiometry case. A higher amount of Mn favours partial oxidation supporting the assumption that Mn is the reactive specie.[28]

The suggested mechanism for methane oxidation in perovskite-oxide is the Mars-van Krevelen one, connected with the presence of a B-site redox couple.[28] The following steps can describe processes involved:[36]

1. Homolytic rupture of C-H bond:

$$H_3C\text{–}H + [O]\,[M^{n+}\ O_m\ ] \rightarrow [H_3C\bullet] + [OH]\,[M^{n+}\ O_m]$$

In the first activation step, C-H bond is broken homolytically. The reaction between C-H bond and a surface bond oxygen leads to the formation of a methyl radical specie.[37] This is the limiting step.

2. Spillover mechanism:

$$[H_3C\bullet] + [M^{n+}\ O_m\ ] \rightarrow [M^{(n-1)+}\ \ O_{m-3}\ CO_2\ ] + [OH_2]$$

In the second step, there is the interaction between the methyl radical specie and the oxygen species on the surface, coordinated by a metal site, M^{n+}, a good electron acceptor.

3. Desorption of products:

$$H_2O \text{ and } CO_2 \text{ desorption (}\textit{slow}\text{)}$$

In the third step, the species formed, H_2O and CO_2 desorb from the sample surface. The elimination of desorbed species is relatively slow, inhibiting the overall rate of the catalytic reaction.

4. Reformation of active species:

$$[M^{(n-1)+}\ O_x\ ] + O_2 \rightarrow [O]\,[M^{n+}O_m]$$

In the last step, the electrocatalytically active site is reformed thanks to the interaction of oxygen. Speed of the last reaction is connected to the oxygen mobility, in surface and oxygen ion conductivity (diffusivity). If the oxygen mobility is not enough, this last reoxidation step become the limiting one of the process.

At intermediate-high temperatures, oxygen mobility does not play an important role, especially using methane as fuel because in oxygen nonstoichiometric perovskite this mobility is always above the minimal value needed.[36] The oxygen mobility from the bulk is not dependent on the quick diffusion along grain boundaries. Instead, it is affected by crystal domain size. Methane access to the active sites is limited by surface area.[38]

Another important factor connected with catalytic activity is the specific surface area (SSA). The main factors that affect catalytic activity are divided in two categories:

- Intrinsic, like composition and crystalline structure,
- Extrinsic, like texture and surface morphology as reflected in SSA value.

In long term stability tests, SSA lowering due to a lower number of active sites, is connected to a lower activity. It can be compensated by oxygen mobility caused by nonstoichiometric composition.[36]

3. LSCM synthesis and characterisation

In this section, it is analysed the method of synthesis used to produce the perovskite of interest, *LSCM*. Moreover, the material is characterised using different techniques to achieve important structural, morphological and chemical information. The results are analysed and discussed in next sections.

3.1 Synthesis

$La_{0.75}Sr_{0.25}Cr_{0.5}Mn_{0.5}O_{3-\delta}$ (*LSCM*) has been synthesised using citrate method also called *Marcilly method*. Reagents have been selected and they are listed: lanthanum oxide (La_2O_3), strontium carbonate ($SrCO_3$), manganese acetate tetrahydrate ($Mn(CH_3CO_2)_2 \cdot 4H_2O$) and chromium nitrate nonahydrate ($Cr(NO_3)_3 \cdot 9H_2O$). La_2O_3 and $SrCO_3$ have been dissolved in nitric acid to obtain the correspondent metal nitrate. Chromium and manganese precursors are dispersed in water to obtain a solution. The stoichiometric quantity of each reagent has been used to prepare the desired perovskite. Solutions are added to citric acid that has been previously dissolved in water. The citric acid is used to obtain the complexation of metal cations. In fact, it is a complexing agent, capable to coordinate metallic cations in three different points of its chain and to interconnect them. Its concentration is 1.9 times the quantity of metallic cations in solution. The pH of the solution is 1. The complexation is possible thanks to the addition of ammonium hydroxide. In this way, a pH of 7-8 is reached. At this pH the third constant of dissociation of citric acid is reached and the complete complexation is achieved. The solution is heated to remove the liquid part, and a wet gel is formed. The gel is heated at 350°C and starts to combust. The powder is now formed. It is heated at 400°C to eliminate all the carbonaceous residue. It is sintered in air 6 hours at 700°C. The temperature of calcination is reached utilising a heating ramp of 6°C/min. An analogous cooling ramp of 6°C/min since room temperature is used. In this way, the dark violet *LSCM* powder of interest is produced.

3.2 Characterisation

3.2.1 X-Ray Diffraction (XRD)

The instrumentation used to produce X-ray diffraction pattern is a Bruker D8 Advance diffractometer with Bragg-Brentano geometry using a Cu K_α radiation (40kV,40mA, λ=0.154nm). The XRD pattern of the powder is reported in *Figure 9*. The measure takes place using 0.03°/step at a counting time of 10 s/step in the range between 20°

and 70°, at room temperature. The phase is identified by the search and match method using JCPDS database. It is possible to see the characteristic peaks of *LSCM*. In particular, the most intense peak is located at 2Θ=32.6° as reported in literature.[34] These peaks are typical of an orthorhombic structure of the perovskite-like phase of interest. The baseline signal is affected by noise, connected with the instrumentation sensibility. There is the possibility of strontium carbonate phase presence in low quantity. The presence of other insulating phases could be detrimental to the conductive characteristic of the anode during electrochemical tests. The peaks of our interest are not perfectly resolved because the calcination process has been made in air. The atmosphere influenced the characteristic of the XRD pattern as it has been previously analysed in literature.[31] Using Scherrer equation to determine the dimensions of crystallites, it can be found that the average crystallite radius is between 15-20 nm in different *LSCM* powder batches. In the case that during synthesis a higher amount of HNO_3 is utilised, crystallite dimension is lower.

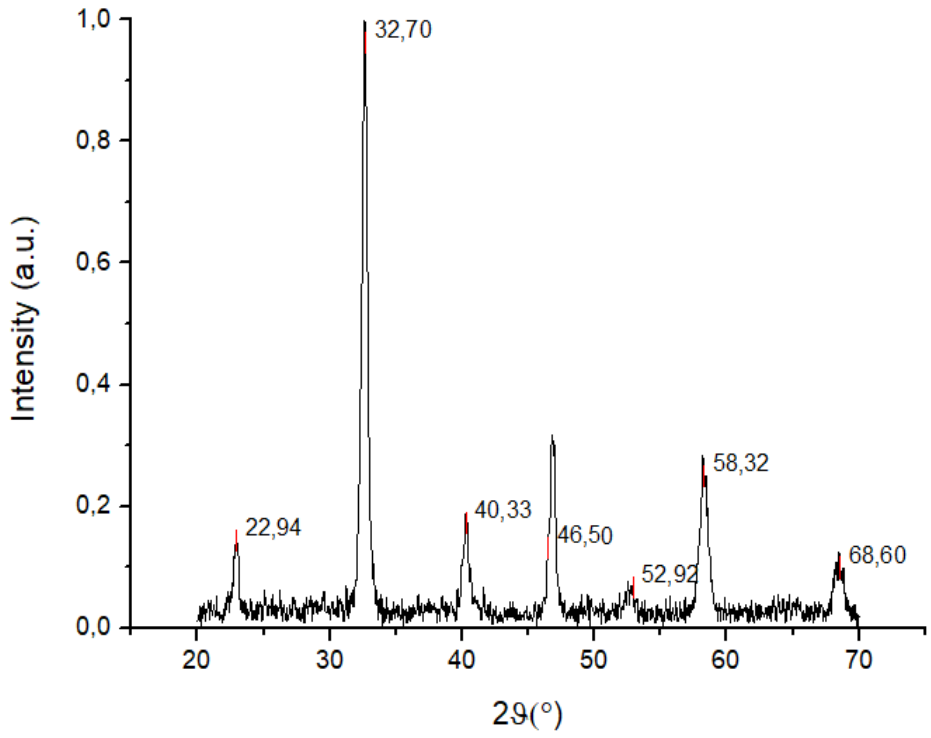

Figure 9. XRD pattern of LSCM powder sintered at 700°C per 6 hours.

3.2.2 Temperature Programmed Reduction (TPR)

H_2-Temperature Programmed Reduction of the powder has been carried out. The data are collected with an Autochem II 2920 Micromeritics. This technique gives information about the species that are reducing at a range of temperature of interest. The 0.05g of powder has been tested in a quartz reactor during a temperature ramp of 10°C/min between 38°C and 898°C under a constant flow of H_2 5% in Ar. The sample was first outgassed in He at room temperature. The temperatures analysed include working range of anodic material during electrochemical tests, and by this analysis is possible to have information about the stability of the material of interest. In *Figure 10*, reduction curve is presented. There is a single gaussian peak centred at 403°C. This temperature is connected with the reduction of the species $Mn^{4+} \rightarrow Mn^{3+}$. The instrumentation gives a consumption of hydrogen of 5.76 10^{-5} mol. This value is in good agreement to the theoretical amount of hydrogen consumed of 5.86 10^{-5} mol during total Mn(IV) reduction to Mn(III). Moreover, the obtained value is of the same order of magnitude of the one reported by Zhang at al. in the case of manganate-based perovskites.[39] There is not a peak at 580°C usually connected to chromium reduction (Cr^{4+}/Cr^{3+}) because chromium is stabile in *LSCM* structure and it maintains six-fold coordination in Cr^{3+} oxidation state.

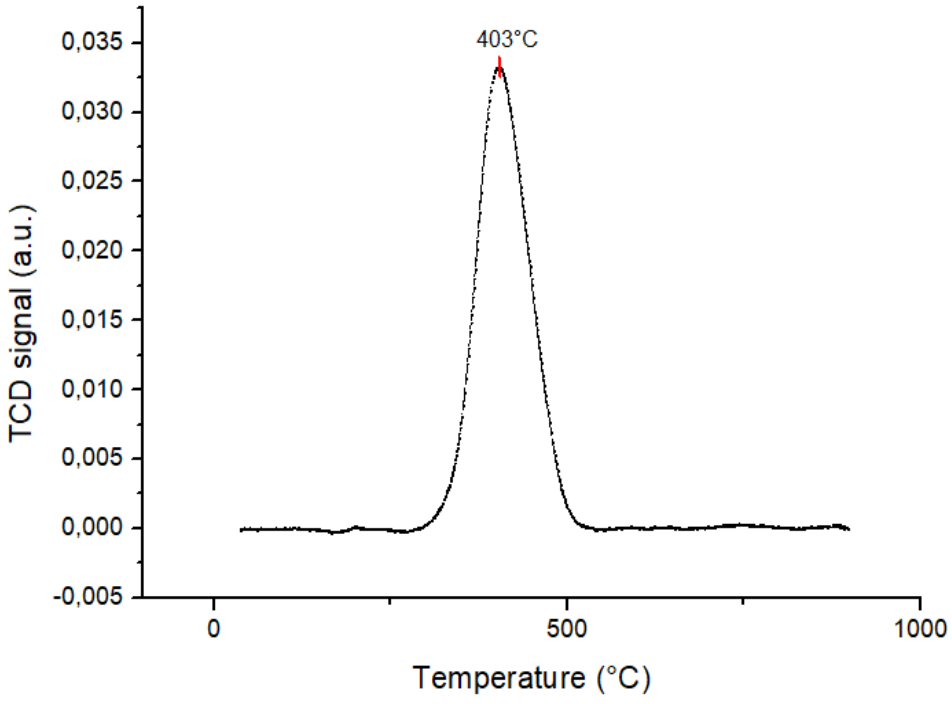

Figure 10.TPR curve for LSCM powder.

3.2.3 Brunauer – Emmett – Teller Surface Area (BET)

The surface area determination of *LSCM* sample is performed using ASAP2020 Plus instrument. Perovskites usually have a surface area not elevated. The calcination temperature can influence the surface area value. Higher calcination temperatures are related to a lower surface area. In fact, in literature the specific surface area for a *LSCM* sample calcinated at 1100°C is 4.59 ± 0.14 m^2/g.[35] The powder here produced, calcinated at 700°C has an estimated surface area measured of 13.0±0.1 m^2/g. This value is in good agreement with literature, in the case of sample calcinated at 700°C and produced by combustion method.[40]

The isotherm linear plot is reported in *Figure 11*.

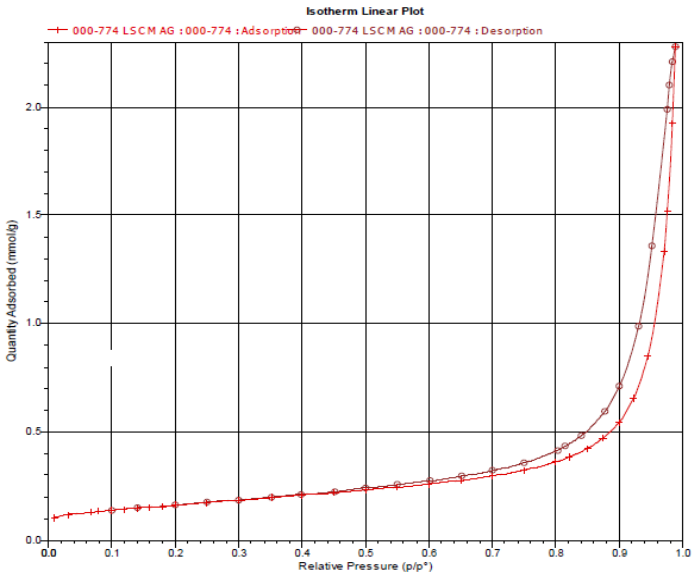

Figure 11. Isotherm linear plot for LSCM sample.

In nitrogen adsorption analysis six types of adsorption curves can be found, using IUPAC classification. The case of our interest can be correlated to a type II behaviour, typical of macroporous structures with stronger interactions with the adsorbate .[41] It can be noted a hysteresis cycle between adsorption and desorption signal. The hysteresis loop can be related to H3 type in IUPAC classification. It represents a solid formed by aggregates or agglomerates of particles forming slit-shaped pores with nonuniform size or shape.[41] This would indicate the presence of a macropore network of the powder assembly and also an interparticle mesoporosity as indicated by the hysteresis loop.

In *Figure 12*, it is possible to see pore width distribution, calculated by BJH (Barrett-Joyner-Halenda) method.[42] There are two dimensions of pores that characterise the sample. In fact, there are two peaks indicating a volume concentration of pores of a certain width. A first peak is correlated to a pore width of 2-3 nm and a second one corresponds to a pore width of 30 nm. The first one can be associated to superficial porosity, using BJH method data for this type of porosity should be interpreted with caution. In fact, Kelvin equation, basis for BJH method is reliable only for pores >2nm because of the approximations utilised[43]. So, the second peak is of higher interest and it can be determined that the average estimated dimension of pores is of 27.1nm.

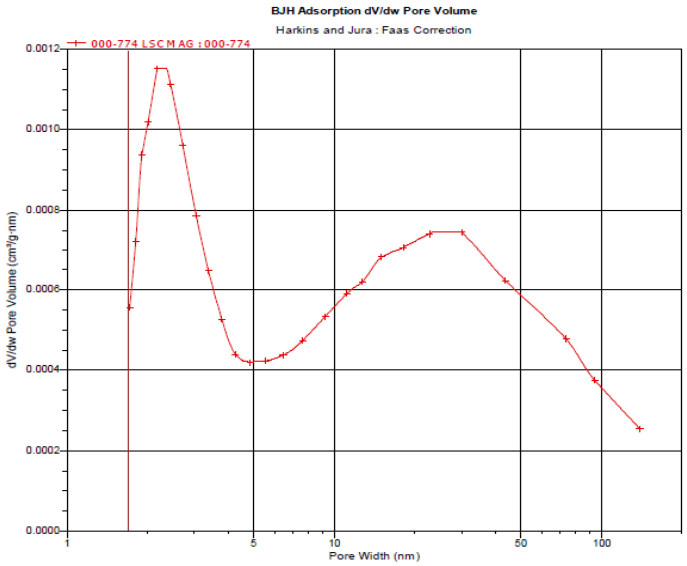

Figure 12. Pore width distribution.

3.2.4 Scanned Electron Microscopy/ Energy Dispersed X-ray Analysis (SEM/EDX)

SEM is made on two different batches of *LSCM*. SEM permits to have information about the morphology of the powder in exam. In the first case, the *LSCM* powder is made utilising a low quantity of HNO_3 during synthesis (LSCM1), instead in the second case the amount of HNO_3 is higher (LSCM2). In LSCM1 sample, the powder is thinner. This fact is also visible in the SEM image below (*Figure 12a*). The structure is lamellar and not dense. The second sample, LSCM2, is a powder of higher density as can be seen in the SEM image (*Figure 12b*). In both the samples, the porosity is enough to permit the flow of gas, during electrochemical tests. This can guarantee a relative low resistance to transport of gasses through the enhancement of TPB.

(a)

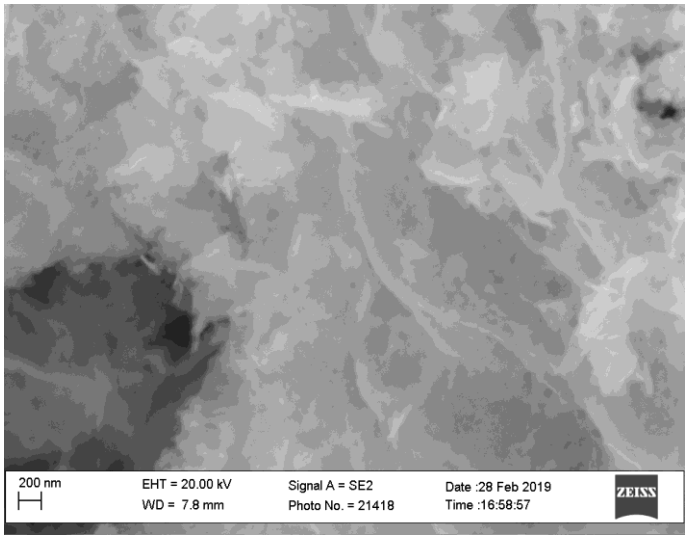

(b)

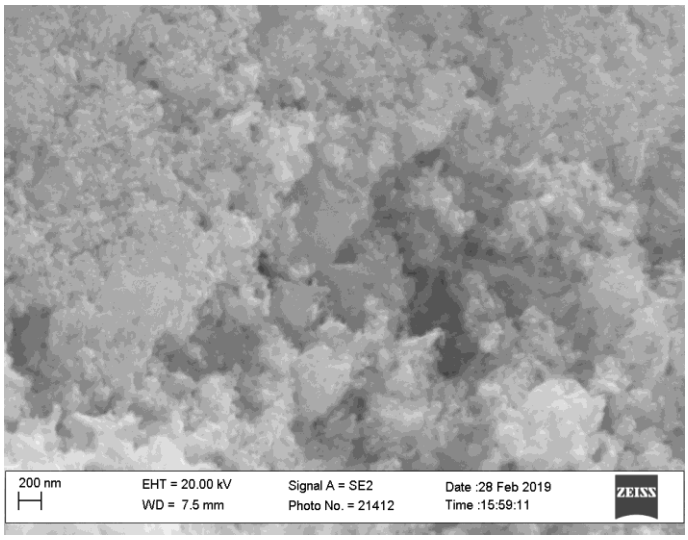

Figure 13. SEM images taken at 20.00kV and 25k of magnification. (a)LSCM1 (lower amount of nitric acid) (b)LSCM2 (higher amount of nitric acid).

Moreover, EDX has been made to quantitatively analyse elements concentration under the superficial layer. In particular, for each sample, it is calculated the average atomic percentage of each cation and it is confronted with the stoichiometric value. The calculated concentration (%) for each element is listed in this table, *Table 1*.

Table 1. EDX cation concentration (%) for LSCM1 and LSCM2 and theoretical values.

	LSCM1	**LSCM2**	**Theoretical value**
Element	*Concentration (%)*	*Concentration (%)*	*Concentration (%)*
La	34.9	29.9	37.5
Sr	15.3	23.9	12.5
Cr	19.5	20.5	25.0
Mn	30.3	25.8	25.0
Cr/Mn	0.64	0.79	1.00
Sr/La	0.43	0.80	0.34

The percentage of chromium in both samples is lower than the stoichiometric one. In the second sample, the percentage of strontium is elevated this can be due to a partial agglomeration of strontium. Also, lanthanum presence is lower than the theoretical one. This can be correlated to higher strontium presence. Differences in concentration in the two samples can be connected with synthesis conditions. In fact, higher amount of nitric acid means higher amount of ammonia to increase pH. This can cause a more violent self-combustion favouring the diffusion of strontium toward surface and the formation of oxides or carbonates.

3.2.5 X-ray Photoelectron Spectroscopy (XPS)

XPS gives important information about the quantitative presence of each element on the surface of the sample. Moreover, photoelectron lines position can be discussed.

To analyse these samples, it is necessary to understand the adequate X-ray source. The choice is between K-α emission of Al and the one of Mg. Comparing the binding energy of photoelectron lines for each element with the energy position of Auger lines that depends on the source utilised, it is possible to avoid eventual overlap.

In the case of *LSCM*, it is possible to use K-α line of Al as X-ray emission source. For each element, it is selected a region in binding energy in which the most intense photoelectron peaks usually stay. Peaks are then associate to an orbital of the element of interest. The spectrum is taken utilising high resolution acquisition setup, associated to a passing energy of 23eV. Only carbon impurities can be revealed, their presence is due to superficial contamination of the samples.

XPS reveals superficial cation concentration for two *LSCM* samples prepared. Element concentration is estimated utilising area evaluation of the most intense photoelectric peaks. Baseline is calculated by the software utilising the Shirley method, after operator evaluation of peak extremities.

Elements concentrations estimated with XPS are listed in *Table 2*.

Table 2. XPS cation concentration (%) for LSCM1 and LSCM2 and theoretical values.

	LSCM1	**LSCM2**	**Theoretical value**
Element	*Concentration (%)*	*Concentration (%)*	*Concentration (%)*
La3d	39.9	43.6	37.5
Sr3d	12.6	12.2	12.5
Cr2p	12.1	16.8	25.0
Mn2p	35.3	27.4	25.0
Cr/Mn	0.34	0.61	1.00
Sr/La	0.32	0.28	0.34

Lanthanum and Strontium superficial concentration in both the samples is in good agreement with the theoretical value. In the case of chromium, the superficial concentration is less than the theoretical one, instead manganese concentration is higher. In general, it can be observed that the higher concentration of nitric acid causes the surface segregation of lanthanum while lower concentrations favour the surface segregation of manganese.

These data can be confronted with the ones of EDX. It is possible to affirm that, when high amount of nitric acid is used, lanthanum concentration is higher in superficial layers analysed by XPS, consistently strontium appears segregated under the surface (deeper sampling with EDX). Manganese is surface segregated in the sample treated with less nitric acid and the segregation interests a deeper layer (in fact is observed both by XPS and EDX).

Considering the Sr/La ratio and Cr/Mn ratio for both the samples and techniques utilised, it can be noted that chromium is present in a lower amount with respect to the nominal value, independently on the amount of nitric acid.

In the case of La, XPS spectrum between 853-827eV is presented in *Figure 14*. Peaks between 840-830 eV are connected to La^{3+} $3d_{5/2}$ orbital. Another doublet can be found at higher Binding energy between 845-860 eV and can be correlated to La^{3+} $3d_{3/2}$.

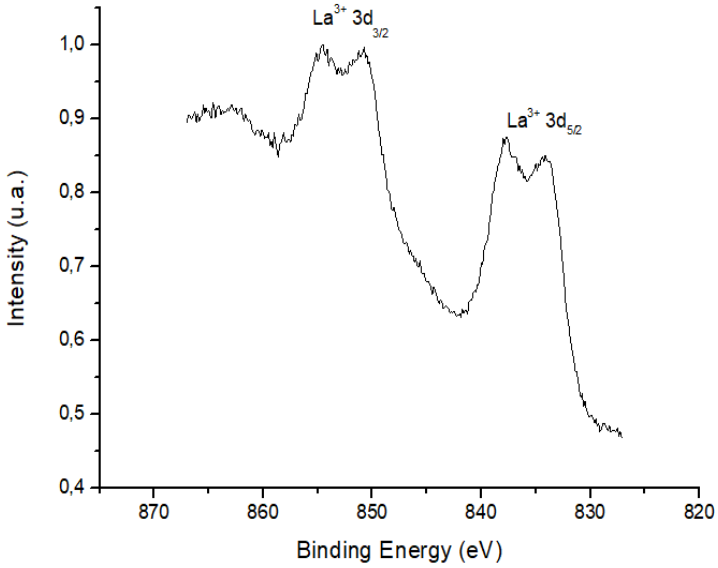

Figure 14. High resolution XPS spectra of La3d orbital for LSCM sample.

In the region between 147-126 eV, Sr^{2+} peaks can be found. The single peak can be deconvolved into two peaks correlated to Sr^{2+} $3d_{5/2}$ orbital at 133eV and Sr^{2+} $3d_{3/2}$ orbital at 136eV; these values agree with how expected for Sr perovskites. The spectrum is reported in *Figure 15.*

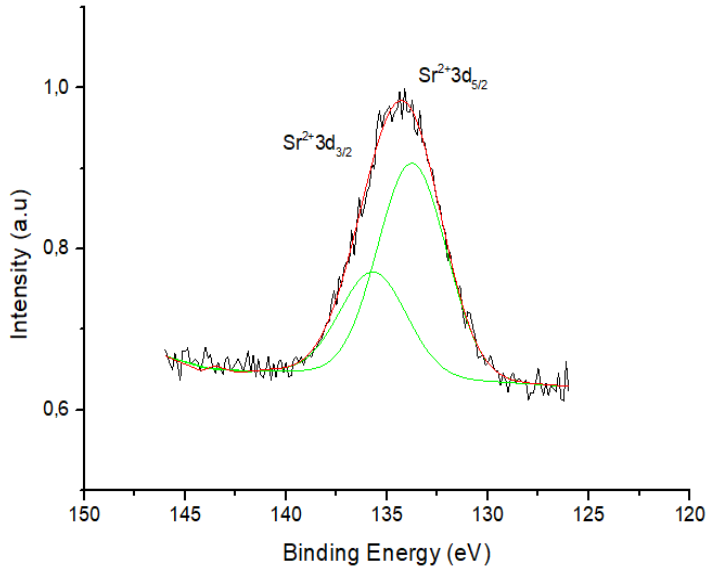

Figure 15. High resolution XPS spectra of Sr3d orbital for LSCM sample.

The spectrum in *Figure 16*, represents the single peak due to Oxygen, 1s orbital. The main information obtained from the analysis of this peak is that O is present inside the *LSCM* structure as expected and no significant surface contamination is observed.

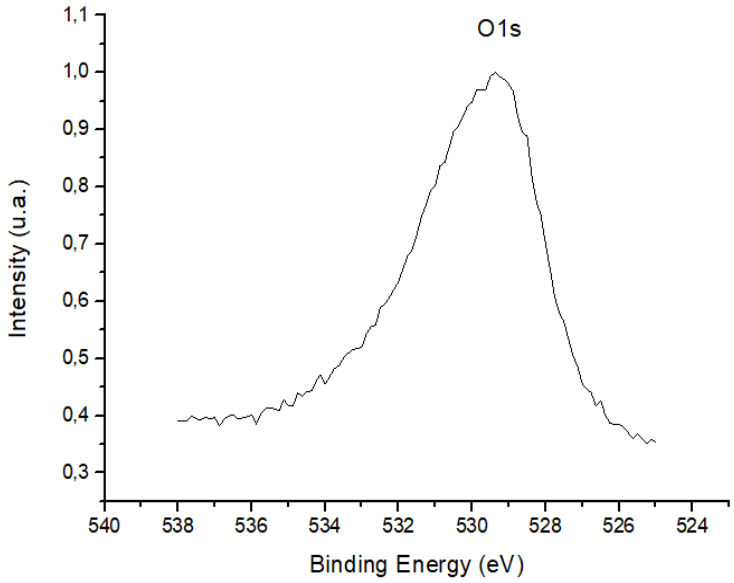

Figure 16. High resolution XPS spectra of O1s orbital for LSCM sample.

Cr 2p signals are observed between 607-565 eV, see *Figure 17*. Peaks between 582.50-571.00eV can be connected to Cr^{3+} $2p_{3/2}$ (576eV) and Cr^{6+} $2p_{3/2}$ (579eV) orbitals. While peaks in the region between 594.70-583.40eV are correlated to Cr^{3+} $2p_{1/2}$ (586eV) and Cr^{6+} $2p_{1/2}$ (589eV) orbitals.

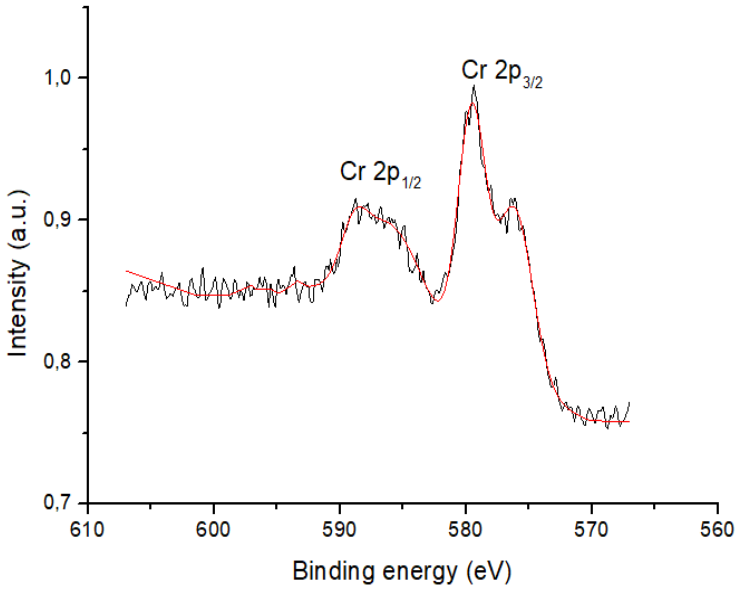

Figure 17. High resolution XPS spectra of Cr2p orbital for LSCM sample.

Finally, Mn 2p peaks are located at binding energy between 632-673eV, see *Figure 18*. Peak at higher binding energy, between 660.70-648.50 eV, is related to Mn^{4+} $2p_{1/2}$ (653.70eV) and Mn^{3+} $2p_{1/2}$(653.20eV) orbital, instead the one at lower binding energy, between 647.40-636.20 eV, is connected to Mn^{4+} $2p_{3/2}$ (643.40eV) and Mn^{3+}

$2p_{3/2}$(642eV). From XPS data is not possible to determine the contribution for each specie to peak intensity. This is due to the fact that the photoelectron lines for Mn^{3+} and Mn^{4+} are localised at binding energies that differ for less than 1 eV and are not distinguishable.

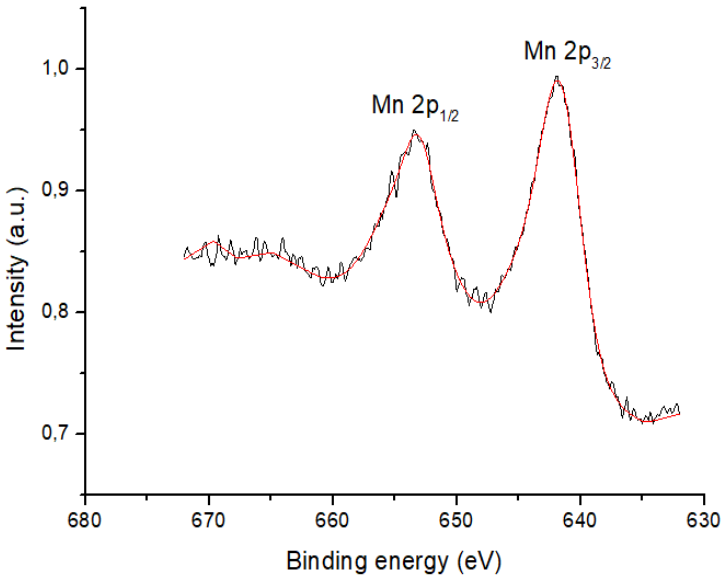

Figure 18. High resolution XPS spectra of Mn2p orbital for LSCM sample.

4. Cell study of LSCM

In this contribution, electrolyte supported symmetric cells are prepared. The focus is on electrode material. Maintaining the same electrolyte support, different electrode materials have been tested: composites and impregnated electrodes. The comparison between the obtained results allows to evaluate which is the procedure capable to assure the higher electrochemical performance. Moreover, beside this, the EIS study allowed to better define and investigate the phenomena characterising anode behaviour under hydrogen or methane atmosphere.

4.1 Stack design

Different type of cell construction can be utilised. In particular, a stack can be arranged using tubular or planar design. In this way a high number of cells can be linked to achieve an adequate voltage output useful in practical applications.

Tubular SOFC

The stack consists of a bundle of single cell tubes. Usually the anode material (supported anode, see *Figure 19*) forms a tube, closed at one end. Electrolyte and cathode layer are overlapped on the outside of the tube.[9] Gas flow is arranged to have oxygen flux inside the tube and fuel flux outside. In addition, the electrical connections design a path to connect in series cells that form the stack. Also, cathode supported cells can be used.

Tubular cells are more tolerant to stress from internal reforming than planar ones. They permit the construction of a dense packaging of cells, reducing radius of the single tubular element. Also, a high number of electrical connection points can be inserted.

The main disadvantage is the cell construction and design. The current path is usually so long that the power density can be negatively compromised. Fuel cell system equipped with fuel cell bundles can handle loads from 100W up to 4.5kW.[17]

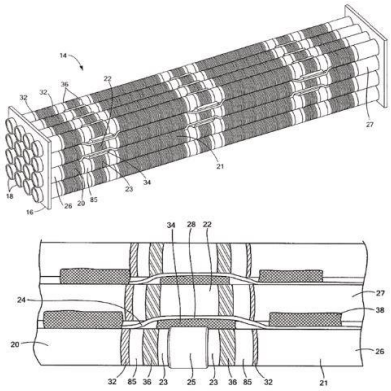

Figure 19. Bundle package of anode-supported tubular cells (14—fuel cell bundle; 16—cell holding manifold; 18—fuel cell; 20, 21, 26, 27, 32—cathode; 23, 22—interconnection; 24— current collector; 25—interconnection clip; 34—insulator; 36—interconnection material in contact with inner anode; 85—uncovered electrolyte gap).

Planar SOFC

In planar design, the single cell is formed by flat plates which are connected in electrical series. Different type of support can be used, as it is discussed in the next sections. The plates can have rectangular or circular form. Planar SOFC stacks have to possess an adequate design to support mechanical and thermal stress. Moreover, heating and cooling processes, gas flow uniformity and gas access have to be optimised to achieve the performance of interest. Also, the electrical link between single cells in the stack has to be taken in account.[17] An example of planar SOFC configuration is proposed in *Figure 20*.

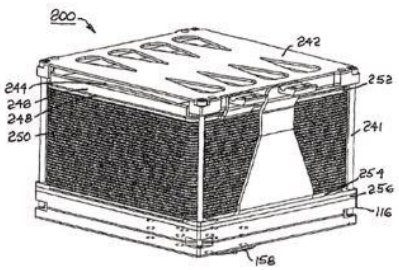

Figure 20. SOFC stack by Delphi (116—gas distribution manifold; 158—flange for attaching to a system of manifolds; 200—fuel cell stack module; 241—spring loading bolds; 242, 244— spring plates; 246—load pressure plate; 248—electric insulator; 250—fuel cell stack; 252— positive current collectors; 254—negative currents collectors; 256—seal; 254—bonding interconnector).

4.2 Cell configuration

In this work, a planar cell is prepared. There are several possible designs for a planar SOFC construction. Electrolyte, cathode and anode can be arranged in different ways to achieve an adequate mechanical strength and performance. The layer that possess mechanical strength in a fuel cell is called support. The resistance of a layer is inversely proportional to the thickness: it is thus necessary to find a compromise between conductivity and strength. The principal cell configurations are here reported.

The electrolyte-supported configuration is the one used in this work to test cell electrochemical properties. This choice has two motivations; at first the electrolyte-supported cell is easier to realize in laboratory. Moreover, this work is focused on anode design and optimization whereas the implementation of the whole cell performance will constitute a further step. Other designs can be used in which anode, cathode, interconnect or a dedicated metallic layer act as mechanical support. This strategy allows to decrease the thickness of the electrolyte and to obtain lower ionic resistances and higher power values.

Electrolyte-Supported SOFC (ES-SOFC)

It is the first setup used. It is composed by a thick, dense electrolyte, the support, sandwiched between cathode and anode porous layers. The electrolyte layer has to be dense to avoid the mix of fuel and air and has to be a pure oxide ions conductor. Increased thickness guarantees electric insulation and gas separation, but higher ionic resistance reduces the cell performance. [17] To minimise electrolyte ohmic loss, higher operating temperatures are needed.[9] The ES-SOFC configuration can be schematised as in *Figure 21*.

Figure 21. EC-SOFC configuration.

Anode-Supported SOFC (AS-SOFC)

In this configuration, anode is the supporting layer, as can be seen in *Figure 22*. To guarantee an adequate functionality and presence of triple phase boundaries, the anode layer has to be sufficiently porous. This fact gives an adequate

Figure 22. AS-SOFC configuration.

flexibility to the cell system, while it is difficult to create a dense electrolyte layer over the anode.[17] A thin electrolyte permits lower operating temperature. There are some problems due to potential anode reoxidation and mass transport limitation in thick anode.[9]

Cathode-supported SOFC (CS-SOFC)

In this case the cathode is the mechanical supporting layer. It leads to a lower in operating temperature thanks to a thin electrolyte but there is a lower conductivity and mass transport limitations due to a thick cathode.[9] The scheme of this configuration can be seen in *Figure 23.*

Figure 23.CS-SOFC configuration.

Metal-Supported SOFC (MS-SOFC)

Another option is the utilisation of a support made of a metal (*Figure 24*). The metal layer gives good mechanical strength, it can simplify cell stack manufacturing. It is located on the anode side and it is highly porous and permits fuel access. Some challenges are connected to make a good correlation between TECs of different layers. [17]

Figure 24 MS-SOFC configuration.

Interconnect-supported SOFC (IS-SOFC)

The structure of the cell is supported by the interconnect material, as in *Figure* 25. This configuration leads to a reduction in cell components thickness. There are some problems related to interconnect oxidation and flow field design limitations.[9]

Figure 25. IS-SOFC configuration.

4.3 Ink preparation

The first step for cell preparation consists in verifying the compatibility between electrode powder and electrolyte material. This part will be described in next sections testing both LSGM and YSZ as electrolyte. These electrolytes have been chosen because YSZ has elevated ionic conductivity and low porosity instead LSGM use permits lower working temperature avoiding SOFCs disadvantages connected to thermal stability.

The second step is the deposition of an electrode-based ink on the electrolyte. In the present case the ink constituted by the anodic material is applied over the electrolyte using tape casting technique.

A pellet of electrolyte is obtained utilising a press. The starting material for the electrolyte pellet is a commercial powder of LSGM or YSZ. The pressure to be applied was optimized for each electrolyte and resulted of 3 tons and 2 tons respectively to produce YSZ and LSGM pellets. Their diameter is of 25 mm before sintering. The electrolyte pellets are then treated in an oven for 6 hours at 1500°C in air, using a ramp of 5°C/min since 1100°C and a ramp of 3°C/min since 1500°C (these values have been optimized). The cooling ramp is of 5°C/min. Pellets are cleaned and polished utilising ethanol and an ultrasonic bath, to achieve surficial uniformity.

Ink is made from 1g of *LSCM* powder mixed in a mortar with the 3wt% of soot. The function of the soot is to give the adequate porosity to the anode after a thermal treatment. Then, a vehicle resin made of a commercial polymer binder is mixed. The quantity of vehicle in correlation of the powder is of 1:2 in weight. It is used to obtain the appropriate viscosity of the final ink. To adjust the fluidity of the paste, a commercial filler is added in the amount of some drops utilising a pipette. Both vehicle and filler are α-terpineol based. The ink is then deposited on the centre of the electrolyte pellet using a mask of 12 mm in diameter. It is deposited homogenously on both sides and in the pellet centre in a quite reproducible way. The pellets are then thermally treated in different modes, depending on the ink and electrolyte, to optimise the adhesion. This is discussed in next sections. Ink deposited inside a vial after its preparation is visible in the photo, *Figure 26*.

Figure 26 Photo of LSCM ink deposited inside a vial before its tape casting over electrolyte pellets.

4.4 Experimental setup

After ink deposition, cells are then electrochemically tested in a measurement setup shown in *Figure 27*. The system is composed by a tubular oven that in the middle has a cavity for the sample. The sample is pressed between two α-alumina DEGUSSIT AL23 cylinders. In fact, α-alumina tubes can resist to the high temperatures reached during measurements. The cell is electrically connected, thanks to a deposited conductive paste, to a platinum wire on each side. The cell is then glued to the alumina tube borders using a Magnesium based CERAMABOND; this step is particularly important because has to guarantee the sealing of the electrode compartments and to avoid gas leaks. Inside each Alumina cylinder is injected a gas mixture by means of apposite junctions realised in AISI 316, an austenitic steel with molybdenum alloy that can resist to high temperatures and corrosive gas. The temperature inside the tube is controlled via a K-type thermocouple inserted in one of alumina tubes. To test electrochemical performances, cell is thermally treated using a ramp of 2°C/min above 800°C and stops for 1 hours at this temperature. Then, the cell is tested at lower temperatures. The composition of the gas mixture can be selected and optimized by means of mass flow controllers. EIS (Electrochemical Impedance Spectroscopy) is studied at different temperatures and gas compositions to understand electrochemical processes that take place. As fuel, hydrogen (10% in Ar) and methane (10% in Ar) have been used.

Figure 27. Images of the experimental setup. On the left, there is the oven inside which measurements take place, it is also visible one of the thermocouples used in the apparatus. On the right, the two alumina tubes are presented.

4.5 Electrochemical Impedance Spectroscopy (EIS)

Electrochemical Impedance Spectroscopy (EIS) is a technique that permits the characterisation of electrical proprieties of materials and interfaces.[44] In the EIS studies the cell system is perturbed by an alternating signal of small amplitude: the way the perturbation modifies the steady system and the response is observed.[45] Thanks to the fact that the electrode-material system proprieties are time-invariant, their relations, their dependence by temperature, atmosphere, applied static voltage or current bias can be studied by EIS technique. Microscopic proprieties like the electronic conduction, the electrode transfer between electrolyte and electrode layer and the flow of charged atoms via defects in the electrolyte can be analysed.

Usually a single-frequency voltage or current is applied to the interface and a low-tension signal with alternating varying frequency (ω) is overlapped to it. The phase shift and amplitude of the resulting current to the interface is the parameter of interest. The frequency range applied is about from 1mHz to 1MHz. Electrochemical cell response represented by impedance data in function of frequencies, Z(ω), is approximated to the one of an equivalent circuit made of ideal resistors, capacitors, inductances and various distributed circuit elements. The impedance is composed by a real and an imaginary term, the real part is usually connected with a resistive response, instead the imaginary part to a capacitive one. A resistance can represent a conductive path and it can take account for bulk conductivity or the chemical steps related to electrode reaction. Ideal resistors can be described by Ohm law and are independent by frequency. Capacitances and inductances are related to space charge polarization regions and with specific processes at electrode.

The major disadvantage of EIS is ambiguity of interpretation. Ideal circuit elements are inadequate to describe the electrical response. Z(ω) cannot be approximated by the impedance of an equivalent circuit with only a finite number of ordinary elements. In fact, electrochemical systems usually have a complex behaviour that cannot be associated to ideal resistor behaviour. Capacitive and inductive phenomena are in fact function of frequency in contrast to resistive ones. To describe real system, it is necessary to use no-real circuit elements, as constant-phase elements (CPE) that take in account microscopic material proprieties distributed as in not-uniform solid

electrode-solid electrolyte interface and Warburg elements that can describe diffusion-limited behaviours.

The Nyquist plot is used to describe the electrochemical elements and to create the model circuit to understand the system behaviour. In this kind of plot the real part of Z ($Z_{re}(\omega)$) is plotted on the x-axis and imaginary part on the y-axis ($Z_{im}(\omega)$). Moreover, by Bode plot, frequency response of the system is analysed. In Bode plot, the phase of the signal or the logarithm of the modulus of Z are plotted in function of the logarithm of the frequency. Through them, information about the characteristic frequency of a determined process and how it varies with experimental parameters like atmosphere composition and temperature is studied. For every experimental impedance plot a model circuit is associated and the most important phenomena inside the electrochemical system are analysed.

EIS characterisations were performed using a PGSTAT 302 Autolab Frequency Response Analyser. Measurements have been taken at steady state in the frequency range between 10^{-3}-10^{6} Hz and with signal amplitude of 50mV. The temperatures analysed are from 830°C to 680°C. Each testing temperature is maintained for 1 hour to verify the assumption of stationary state and the reproducibility. This temperature range has been chosen in relation to electrolyte characteristics.

4.6 LSCM/YSZ device

4.6.1 Compatibility with the electrolytes

To test the compatibility between YSZ and *LSCM*, a sample composed by a mix 50:50 in weight of YSZ and *LSCM* is treated 6 hours at 1200°C. From diffraction pattern, *Figure 28*, it is possible to see that there is not formation of other phases. So, compatibility problems or formation of insulating phases at temperature of cell operation can be excluded.

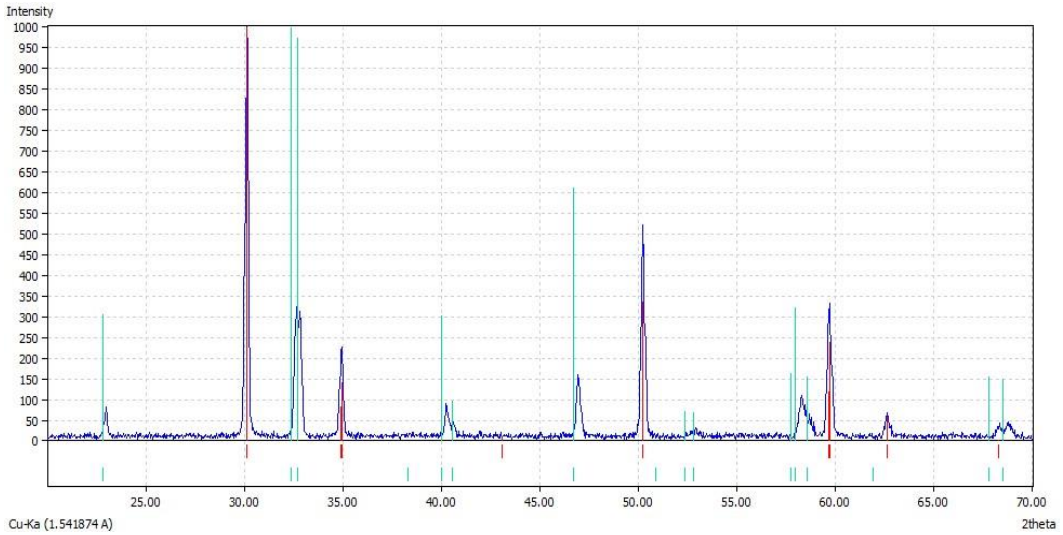

Figure 28. XRD pattern of 50wt% YSZ and 50wt% LSCM sample. Red lines indicate YSZ peaks from database, and green lines indicate LSCM peaks.

4.6.2 Electrode ink

An ink using *LSCM* powder is prepared as described in *Ink preparation*. A first set of cells is made by depositing the ink with the tape casting technique. The thermal treatment is composed by a heating ramp of 3°C/min until 1200°C. This temperature is maintained for 2 hours and then a cooling ramp of 3°C/min is used to reach room temperature. There is not good adhesion of the ink over the pellet, as can be seen in *Figure 29*.

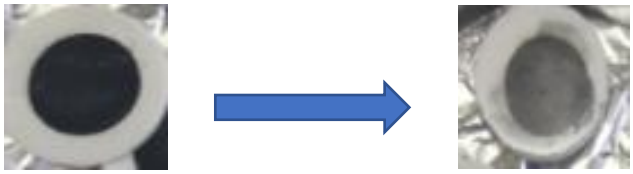

Figure 29. A cell LSCM|YSZ|LSCM before (a) and (b)after adhesion verification. It can be noted that the ink is easily eliminated.

To optimise the adhesion, a new composite ink was created. It is composed of 50:50 in weight of *LSCM* and YSZ. To prepare it, the same method as described previously is used. This time over the pellet on both sides is deposited a layer of the ink of 50wt%*LSCM*:50wt%YSZ. This first composite layer has been deposited to improve adhesion of the superficial ink characterized by a better conductivity. The pellet is then dried at 100°C for 30 minutes and a second layer of ink made only of *LSCM* is deposited. The same thermal treatment described before is performed. Also, in this case the adhesion of the superficial layer is not sufficient even if the 50:50 layer is well dispersed on the YSZ pellet.

A further attempt to improve adhesion was to modify the thermal treatment. The same cell with layered inks is calcinated using a heating ramp of 1°C/min since 400°C and this temperature is maintained for 10 minutes. This guarantees a total elimination of the carbonaceous part present inside the ink. Then, it is used a heating ramp of 3°C/min since 1200°C and this temperature is maintained for 2 hours. The cooling ramp is of 3°C/min since room temperature. Also, this time the degree of adhesion of the *LSCM* ink over the YSZ/*LSCM* layer is not adequate.

To overcome problems related to scarce adhesion of superficial ink, the production of a new composite is performed. The ink is composed by 75wt%*LSCM* and 25wt%YSZ mixed in a mortar before using the method previously explained. On both side of the electrolyte pellet is tape casted a layer of this new ink. Now, the cell is dried at 200°C for 30 minutes. After that, a layer of *LSCM* ink is deposited on both sides. The thermal treatment consists in a heating ramp of 1°C/min since 400°C, this temperature is maintained 10 minutes. After that a heating ramp of 3°C/min is used since 1200°C. This temperature is maintained for 2 hours. A cooling ramp of 3°C/min is used to reach room temperature. Even if some progresses have been made, adhesion is not optimised.

After that, a cell with the same ink composition is treated using the same thermal cycle but this time a stopping temperature of 1300°C was preferred. All these attempts allowed, finally, to obtain a very good adhesion between the electrode and the electrolyte. The composite layer 75wt%*LSCM* /25wt%YSZ maintains an adequate stabilisation over the electrolyte thanks to the YSZ contained, instead the superficial layer has a good adhesion thanks to high percentage of *LSCM* component into the

composite ink. This configuration is preferred also because superficial *LSCM* ink can give electronic, ionic conductivity and catalytic activity, the internal ink made by composite *LSCM*/YSZ has an elevated ionic conductivity thanks to the presence of YSZ compound. Moreover, using a composite material benefits derive by the increment of triple phase boundary (TPB) and in specific surface area (SSA).

SEM images have been taken of the cell structure. In *Figure 30* and *Figure 31*, it is possible to see the electrolyte layer well separated from the electrode. Inside the electrode, it is not easy to find a delimitation between the composite ink layer, *LSCM*/YSZ (75:25) and the one of pure *LSCM*. The structure of the electrode has a good porosity in all its length. This is important during the utilisation of the cell because it determines a high TPB and a good diffusivity of the gas inside the cell. Instead YSZ forms a dense pellet. It is an advantage because it can maintain separated gasses in a full cell test. By EDX, it is possible to demonstrate that *LSCM* sample possess a good homogeneity in composition and in agreement with the quantitative values evaluated for the powder. At interface there are some impurities of Ca, K that can be related to impurities inside the oven where the cell is dried between the deposition of different ink layers.

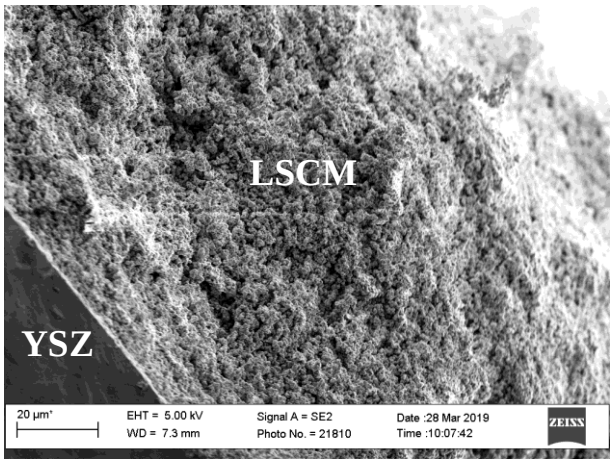

Figure 30. Full cell view taken by SEM, 5.00kV and 2k of magnification. YSZ dense electrolyte (black) and porous electrode layers.

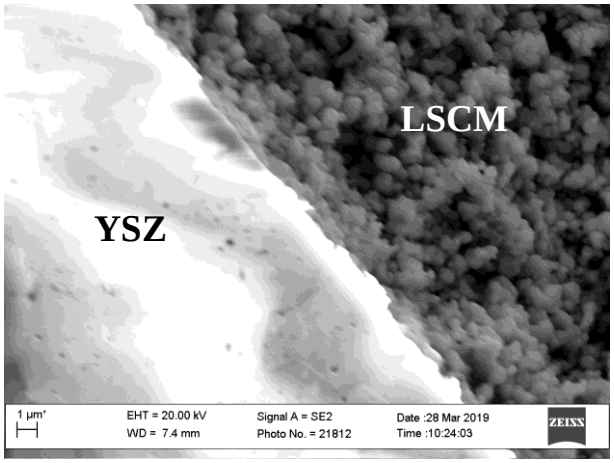

Figure 31. SEM image taken at interface between YSZ electrolyte and composite electrode (75wt%LSCM:25wt% YSZ), 20.00kV and 10k of magnification.

4.6.3 Electron collector

Another problem has been found: the compatibility between ink and gold paste. In fact, the gold paste has been used as electron collector. Gold paste has been deposited over *LSCM* electrodes on both sides by tape casting followed by thermal treatment at 800 °C (heating ramp of 3°C/min). The final temperature is maintained for 2 hours and then a cooling ramp of 3°C/min is used to reach room temperature. After the thermal treatment it is possible to note that the gold layer is not in good state. No adhesion is found, and the electrode superficial layer tends to delaminate, see *Figure 32*. So, it is necessary to use another material to improve electron collector adhesion on the electrode.

Figure 32 Gold paste on LSCM electrode is easily removed. A good contact is not achieved.

Nickel meshes are then selected and applied on the pellet: the needed contact should be assured by the pressure derived from the alumina tubes of the system. The use of only nickel mesh resulted, however, not enough to permit an adequate electric contact. So, *nickel paste* has been considered. The paste is deposited over the electrode ink on both sides using a paint brush. This method has been chosen to permit an adequate contact between the electrode and the platinum wire of the external circuit. After deposition, each cell is thermally treated to stabilise nickel layer. The temperature is raised 2°C/min since 800°C. This temperature is maintained for 1 hour. Next, a cooling ramp of 2°C/min since room temperature is selected.

Tests have also been made using *gold paste added with 5wt% of carbon soot*. This strategy was pursued to obtain a morphology with a higher porosity after calcination at 800°C. Thermal treatment, in fact, is expected to eliminate the carbonaceous component and to permit the formation of pores that should facilitate gas diffusion inside the collector layer.

Other tests have been made utilising a *new gold paste*. It has been deposited with a paint-brush over the electrode layer and thermal treated at 800°C for 1h. The heating and cooling ramp are of 2°C/min. This different gold paste possesses an elevated adhesion over *LSCM* ink. The obtained enhancement in adhesion can be correlated to the new paste purchased and to the decrease of the deposited amount allowed by the use of brush instead of tape casting. In next sections, EIS tests demonstrates that this last solution is the one that permits to reduce ASR values. From impedance analysis, it can be revealed that both nickel paste, and gold paste added with soot give problems connected to gas diffusion and low conductivity. In particular, soot do not form a homogeneous paste if added to gold. After thermal treatment, the conductivity is not elevated and uniform over the electrode. Two activation energy has been found due to different limiting processes at high and low temperature. This behaviour has not been found using the last solution (gold paste) for the electron collector: a single activation energy has been revealed, in agreement with literature. These facts are coherent with the enhancement of conductivity and the improvement of the gas diffusion. So, the measurements in methane has been performed with gold paste deposited as electron collector.

4.7 Hydrogen fuel

In this section, different material has been tested as electron collector utilising hydrogen as fuel and *LSCM* as electrode. EIS response is analysed and the best results have been found using pure gold paste. This is the electron collector chosen in all the electrochemical characterisation that are presented next.

(a) Nickel paste as electron collector

Impedance spectrum has been analysed using a gas flux of 200sccm with 10% H_2 in Ar as fuel. Nickel paste is here selected as electron collector. Electrochemical tests have been performed at these temperatures: 830°C, 800°C, 770°C, 740°C and 710°C. The collected Nyquist plots are reported in *Figure 33.*

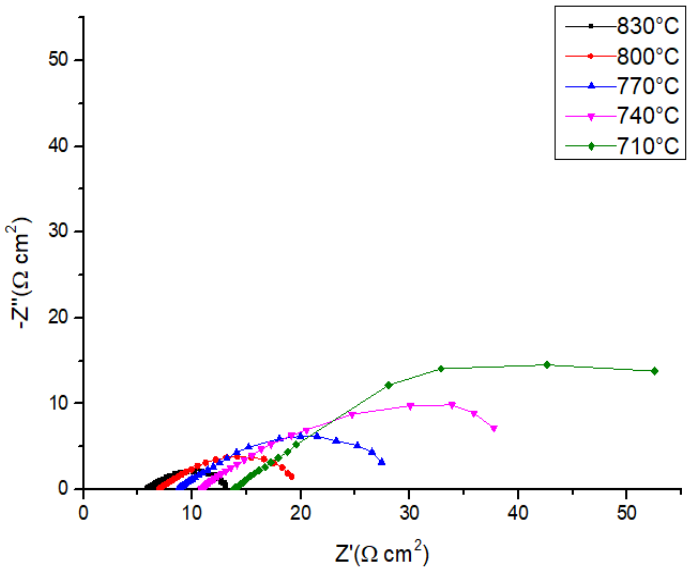

Figure 33. Nyquist plots taken at different temperatures, using 10% of H_2 in Ar as fuel and Nickel paste as electron collector.

Using the program Z-view, an electric circuit can be associated to the processes at different temperatures.

The circuit that can fit each impedance curve, is described as follow, *Figure 34.*

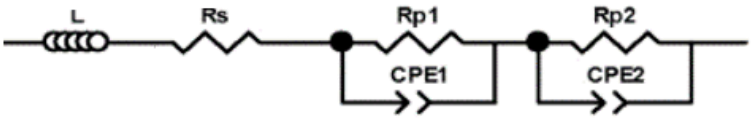

Figure 34. Circuit associated to the impedance curve in Nyquist plot.

L represents the inductance related to the high frequency artefact due to the electric contacts on the experimental apparatus. R_s is the ohmic resistance most due to the resistance of the electrolyte and in a lower part to the one of electrodes, and the contacts resistance associated with interfaces and current collection. The two circuital elements composed by a polarisation resistance (R_p) and a constant phase element (CPE) in parallel corresponds to the two arcs that are described by the impedance curve in Nyquist plot. CPE element is needed to represent frequency dispersion, and it is necessary utilising it in parallel with a resistor to describe depressed semi-circular arcs. Surface roughness and fractal electrode/electrolyte interface can be described by this constant phase element.[46]

R_s, the ohmic resistance associated with the one of electrolyte is lower at higher temperature and starts to increase at lower temperature. It is due to electrolyte characteristic. In fact, YSZ presents a lower ionic resistance at higher temperatures, between 800°C-1000°C.

Observing Bode plot, each process can be associated to a certain frequency. Usually, at high frequencies, above 10^4 Hz, processes due to electrode electrochemistry, in particular to charge transfer reactions or electrical double layer at the two-phase boundaries, are prevalent. The mid frequency impedance at 10-10^4 Hz is associated to a gas-solid interaction as adsorption, dissociation, desorption or to surface diffusion of the adsorbed species. The rate determining step in ceramic based anodes is characterised by an arc with frequencies below 1Hz whose origin is controversial. It is usually related to gas phase diffusion; whose characteristic frequency is between 1-10Hz. However, it can be also originated from gas conversion. Gas conversion impedance can be influenced by test conditions as gas flow rate or composition, temperature or setup geometry. [47] Another explanation to low-frequency process is "chemical capacitance". This contribution is due to the variation in the oxygen non-stoichiometry of the ceramic electrode. It represents the capability of the sample to store chemical energy through oxygen vacancies upon changes in the local oxygen chemical potential.[47]

In the case of *LSCM*, processes at frequencies above 10^4 Hz are not distinguishable in the impedance spectra. This is connected to the fact that the contribute of charge transfer is not relevant. The contribution of mid-frequency processes, at 10^2 -10^3 Hz is significant. It is correlated to gas-solid interaction as adsorption/desorption on surface.[48] The major contribution is at low-frequencies, between 1-10 Hz, and it is usually associated with gas diffusion correlated to electrode microstructure.[48]

From the impedance spectra can be calculated the Area Specific Resistance (ASR) at each temperature. It is the sum of single processes resistance that take place multiplied by the surface area of the electrode and divided by two because it is considered a symmetric cell. In *Table 3* are listed ASR values in relation to the temperature of measurement.

Table 3.ASR values associated to the temperature of measurement.

T(°C)	ASR ($\Omega \cdot cm^2$)
830	7.9
800	11.5
770	17.2
740	28.7
710	37.9
680	47.7

Moreover, the activation energy value (E_a) can be calculated. The value indicates the sum of the activation energies of each physical process that occurs in the electrode.

Ea is calculated by Arrhenius formula:

$$\sigma = \frac{A}{T}\, e^{-E_a/KT}$$

Where A is a constant, E_a the activation energy, K the Boltzmann constant and T the temperature in Kelvin. The logarithm of ASR can be plotted in function of 1/T, expressed in Kelvin. It can be noted that there are two different linear behaviours. They are correlated to two different activated processes dependent by temperature, see *Figure 35.* At high temperature (above T=770 °C) the activation energy is of 1.29±0.01eV. Instead, at lower temperature, Ea corresponds to 0.70±0.01eV.

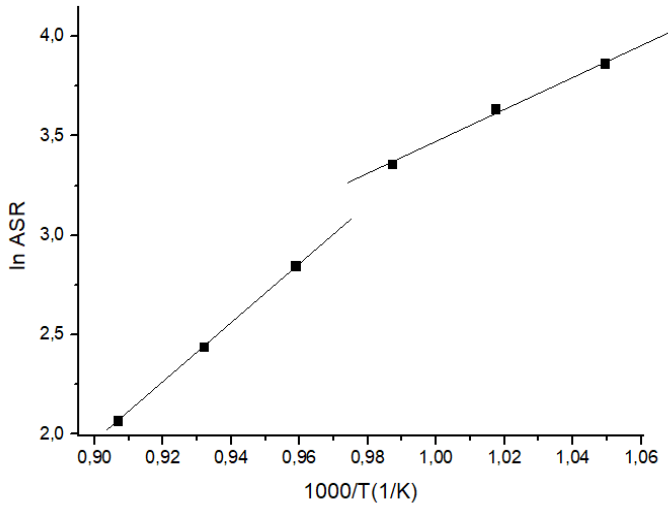

Figure 35. Linear plot of ln ASR in function of 1000/T, with T expressed in Kelvin. Two different linear fitting can be utilised to correlate data at higher and lower temperature.

(b) Gold paste added with 5wt% soot as electron collector

Impedance spectrum has been analysed utilising a gas flux of 200sccm with 10% H_2 in Ar as fuel and gold paste added with 5wt% of soot as electron collector. Electrochemical proprieties have been analysed at 785°C, 760°C,730°C,700°C and 670°C. In *Figure 36*, the Nyquist plots for the temperature range exanimated are compared.

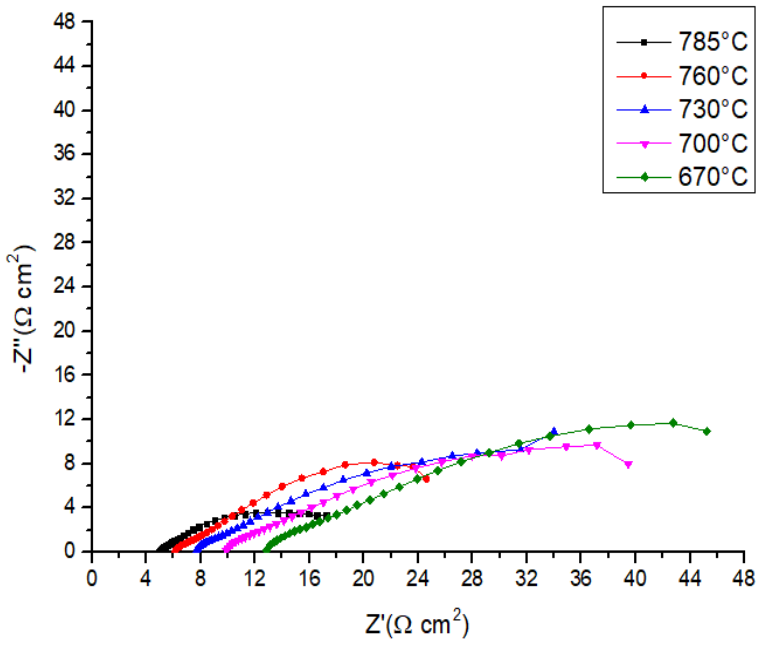

Figure 36. Nyquist plots taken at different temperatures, using 10% of H_2 as fuel and gold paste added with 5wt% of soot as electron collector.

Also, in this case the impedance behaviour can be described as before by a Rs, polarisation resistance due to electrolyte in series with an inductance, L, and two parallel circuits composed by a resistance R and a CPE, see model circuit in *Figure 34.*

R_s, the ohmic resistance associated with the one of electrolyte is lower at higher temperature and increases at lower temperature.

The frequencies associated with the two processes described by R-CPE circuit are of the same order of magnitude of the precedent case. There is a process at high frequencies between at 10^2 -10^3 Hz. The most relevant process is situated at low frequencies between 1-10Hz. The first process is connected to gas-solid interaction as adsorption/desorption on surface and the second one to gas diffusion.

It is possible to associate at each measure an ASR value that describes the sum of the resistive processes possible, normalised by the electrode surface area. These values are listed in *Table 4.*

Table 4. ASR values associated to the temperature of measurement.

T(°C)	ASR ($\Omega \cdot cm^2$)
785	10.5
760	23.3
730	22.9
700	29.2
670	37.0

The logarithm of ASR can be plotted in function of 1/T, with T expressed in Kelvin. By Arrhenius formula, mentioned above, the activation energy can be calculated. Also, in this case, it can be noted that there are two different linear behaviours. They are correlated to two different activated processes dependent on temperature, like in the case of the nickel-based electron collector. At high temperature (above T=760 °C) the activation energy is of 2.2±0.01eV. Instead at lower temperature, Ea is lower and it corresponds to 0.65±0.01eV.

(c) Gold paste as electron collector

Impedance spectrum has been analysed using a gas flux of 200sccm with 10% H_2 in Ar as fuel and gold paste as electron collector. Electrochemical tests have been performed at 830°C,810°C, 780°C,750°C,720°C, 695°C and 655°C. In *Figure 37* the Nyquist plots obtained in the temperature range exanimated, are compared.

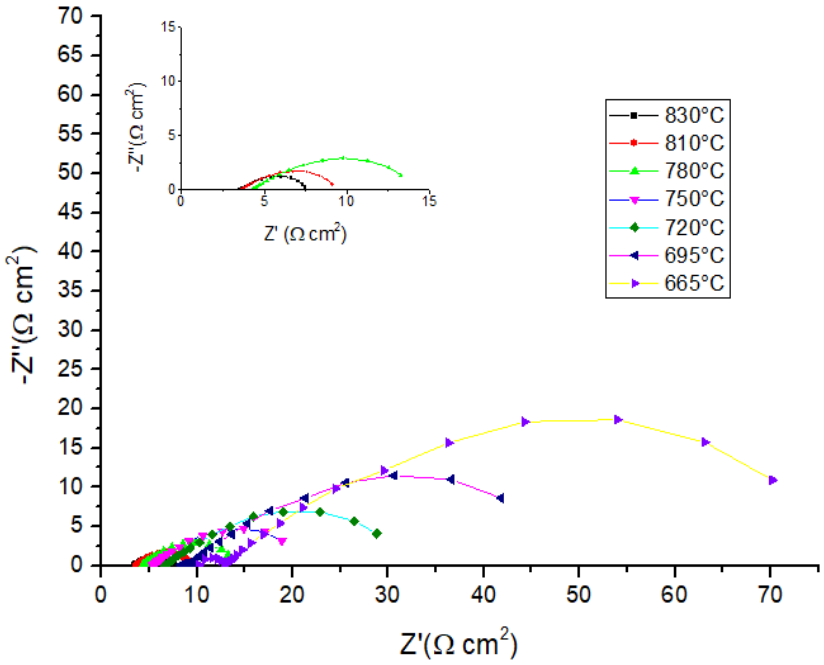

Figure 37. Nyquist plots taken at different temperatures, using 10% of H_2 as fuel and gold paste as electron collector. In the inset, enlargement of the data collected at higher temperatures of 830°C, 810°C and 780°C.

The impedance behaviour can be described, as done before, by a Rs, polarisation resistance due to electrolyte in series with an inductance, L, and two parallel circuits composed by a resistance R and a CPE, constant phase element, see model circuit in *Figure 34*.

R_s, the ohmic resistance associated with the one of electrolyte is lower at higher temperature and starts to increase at lower temperature.

The frequencies associated with the two processes described by R-CPE circuits are of the same order of magnitude of the precedent cases. There is a process at high frequencies between at 10^2 -10^3 Hz and one at low frequencies at 10^{-1} Hz. The first process is connected to gas-solid interaction as adsorption/desorption on surface and the second one to gas diffusion.

It is possible to associate at each measure an ASR value that describes the sum of the resistive processes that take place, normalised by the electrode area. These values are compared in *Table 5*.

Table 5. ASR values associated to the temperature of measurement.

T(°C)	ASR ($\Omega \cdot cm^2$)
830	1.5
810	1.7
780	2.1
750	2.5
720	2.9
695	3.6
665	4.1

The logarithm of ASR can be plotted in function of 1/T, with T expressed in Kelvin. By Arrhenius formula, it can be calculated the activation energy. The logarithm of ASR and 1/T are connected by a linear relation, see *Figure 38*. This fact indicates that takes place a single activated process, characterised by an Ea value of 1.41±0.01eV. This value is in good agreement with the expected one, present in literature of 1-1.44eV.

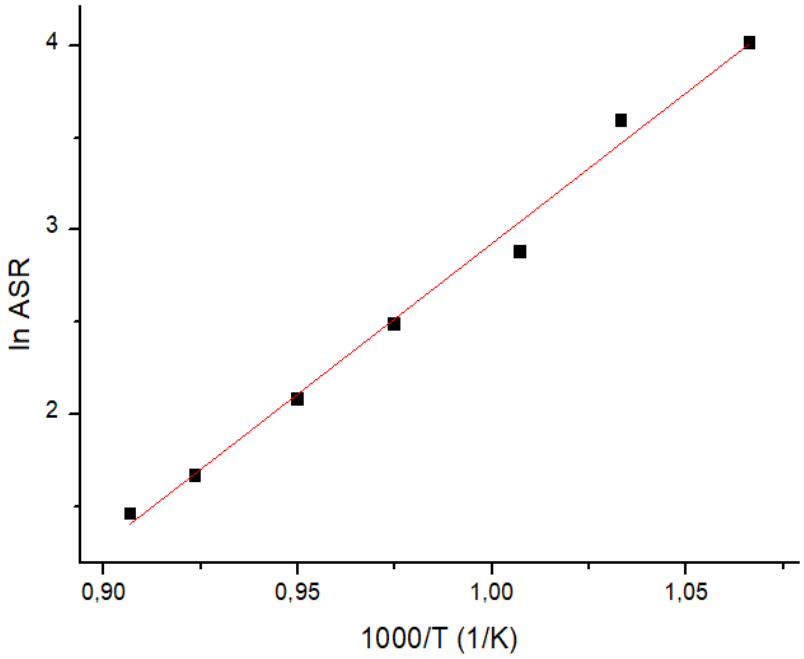

Figure 38. Linear plot of ln ASR in function of 1000/T, with T expressed in Kelvin.

Different hydrogen concentrations have been used. A flux of 200sccm is injected in the experimental setup at a constant temperature of 810°C. Hydrogen percentage inlet is of 5%, 10% and 20% in Ar.

In *Figure 39*, it can be noted impedance spectra taken at different hydrogen percentage.

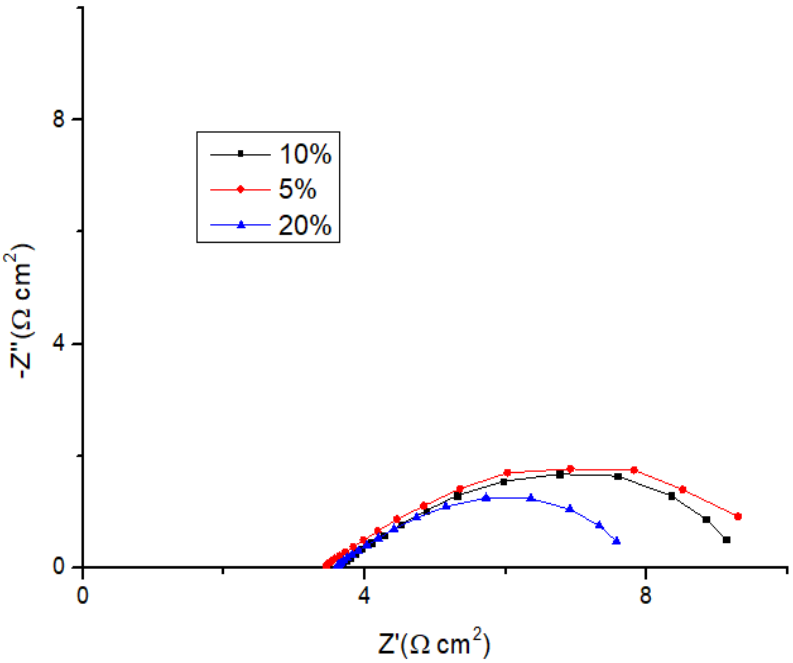

Figure 39. Nyquist plots taken at 810°C, using 5%,10% and 20% of H_2 in Ar as fuel and gold paste as electron collector.

Rs, the ohmic resistance associated with the electrolyte is independent on hydrogen concentration. The model circuit mentioned in the previous sections, reveals that the first process at higher frequencies, connected with the electrochemical performance of the cell, is independent on gas flux. Instead, the low-frequencies process due to gas diffusion has a higher associated polarization value at lower gas flux. This indicates that it is dependent by the gas flux and can be associated to gas diffusion.

Comparing different electron collectors' composition, it has been demonstrated that the use of a pure gold paste deposited by a paint brush not only possesses an adequate adhesion on the electrode but also enhances the measured performance. The same electrode composition and hydrogen gas flux has been tested modifying only the electron collector composition. First, a nickel paste has been deposited using a paint brush, in this case electrochemical performance demonstrated the presence of an elevated ASR and two different activation energies depending on temperature range.

Also, the utilisation of a gold paste added with 5wt% of soot has the same effects. Only the utilisation of a gold paste deposited by a paint brush demonstrates a reduction in ASR values. It is probable that nickel and gold paste added with soot do not possess an adequate electronic conductivity: the use of soot leads to an enhancement into electron collector layer porosity and theoretically this can lead to a reduction of the resistance connected to gas diffusion process. Unfortunately, gold paste and soot tend to separate after mixing resulting in the deposition of a not-continuous and not-homogeneous layer. This leads to an elevated gas diffusion resistive contribution and a performance lowering. All the electrochemical tests have been performed using brash deposited gold paste as electron collector. In fact, this configuration permits to analyse real electrode proprieties, lowering electron collector influence on electrochemical proprieties measurement.

4.8 Methane fuel

Impedance spectrum has been analysed using a gas flux of 200sccm and gold paste as electron collector. To reach the temperature of analysis a gas flux composed by 10% H_2 in Ar is selected. After reaching 830°C, methane is inlet inside the system of measurement and used as fuel. In particular, a 10% of CH_4 in Ar is utilised. Electrochemical tests have been taken at 830°C, 800°C, 770°C, 740°C, 710°C and 680°C. The Nyquist plots for the range of temperature exanimated are compared in *Figure 40.*

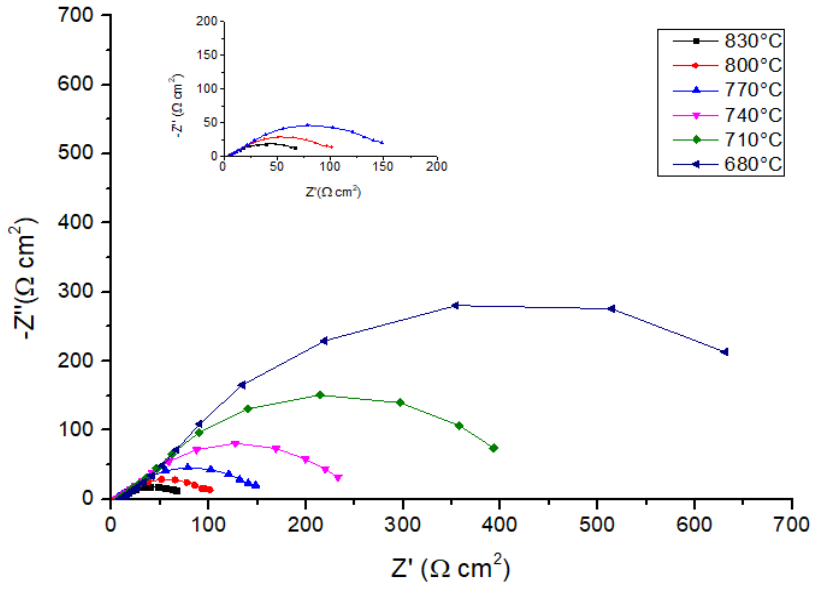

Figure 40. Nyquist plots taken using as fuel methane (10% CH_4 in Ar) at different temperatures. In the inset, enlargement of the data collected at higher temperatures of 830°C, 800°C and 770°C.

The impedance behaviour can be described by a model circuit as the one in *Figure 34*. There are two processes whose frequencies are: for the low frequency one between 1-10^{-1}Hz and for the one at higher frequencies of 10^{3}Hz. The high frequencies process can be related to gas-solid interaction as adsorption, dissociation, desorption or to surface diffusion of the adsorbed species, as mentioned before. The high frequency response is correlated to electronic current exchange and ionic exchange.[49] The low frequency process is usually due to gas phase diffusion or in general to noncharged processes including also oxygen surface exchange. In this case, methane oxidation is dominated by the process at low frequencies.

It is possible to associate at each measure an ASR value that describes the sum of the resistive processes, normalised by the electrode area. These values are listed in *Table 6.* It can be noted that the total polarisation resistance increases due to fuel composition.

Table 6. ASR values associated to the temperature of measurement.

T(°C)	ASR ($\Omega \cdot cm^2$)
830	49.6
800	65.2
770	80.7
740	127.9
710	238.9

The logarithm of ASR can be plotted in function of 1/T, with T expressed in Kelvin. It can be defined a linear behaviour, correlated to a single activated process independent by temperature, see *Figure 41*. Calculated activated energy is: Ea=1.3±0.1eV, this value is in good agreement with literature.[15]

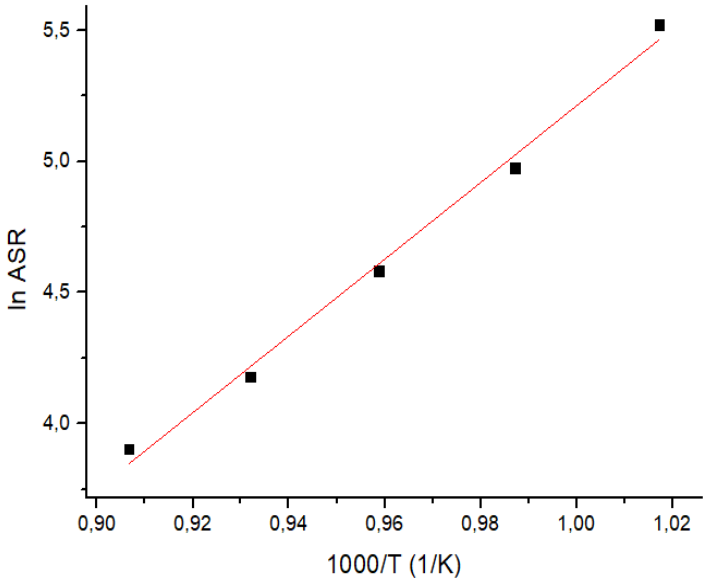

Figure 41.Linear plot of ln ASR in function of 1000/T, with T expressed in Kelvin.

LSCM performance using methane and hydrogen as fuel can be confronted. It is evident an enhancement of ASR value using methane as fuel. This is connected to the fact that *LSCM* is not efficiently active on methane oxidation. To avoid this problem, it can be utilised impregnation of an active specie. Nickel has been chosen in this work to enhance catalytic activity.

Activation energy utilising both hydrogen and methane as fuel is of the same order of magnitude. This is due to the fact that the limiting step in both the cases is the low frequency process. This can be connected to gas phase diffusion contribute. It is related to a not adequate SSA of the electrode. In fact, the ink has been calcinated at 1300°C to achieve electrode layer adhesion on electrolyte and this high temperature reached corresponds to a lowering in surface area. The low frequency process can be also associated to chemical capacitance. So, to lower its resistive contribution also the possibility of depositing an ionic conductive specie on *LSCM* could be exploited.

4.9 LSCM/LSGM device

4.9.1 Compatibility with the electrolyte

Before the utilisation of this electrolyte, a compatibility test has been made. A sample made by a mix 50:50 in weight of LSGM and *LSCM* is treated at 1200°C for 6h. XRD pattern of the sample is proposed in *Figure 42*. There is not presence of other detrimental phases, so the cell preparation is tempted.

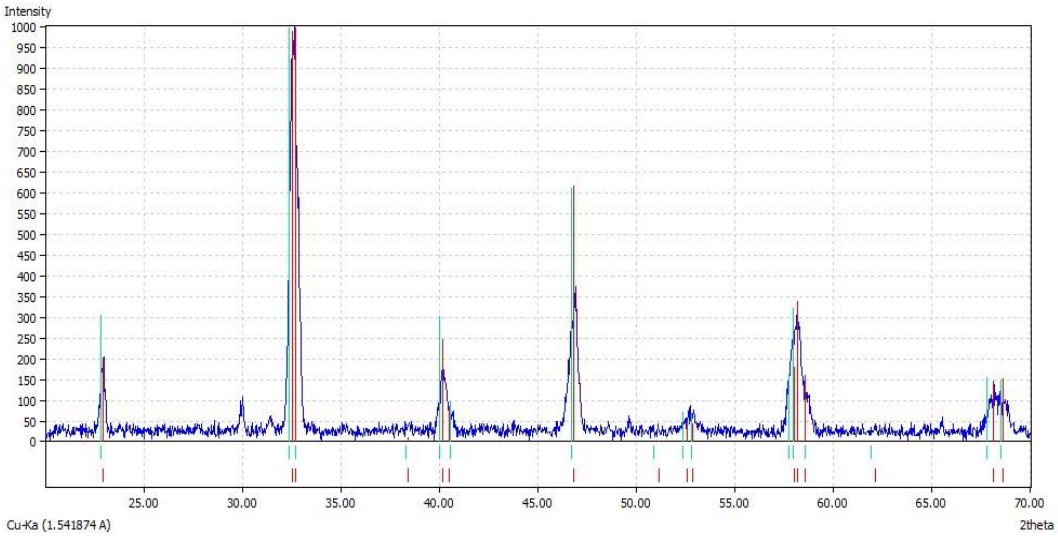

Figure 42. Diffraction pattern of 50wt % LSGM and 50wt % LSCM sample. Red lines indicate LSGM peaks from database, and green lines indicate LSCM ones.

An ink using *LSCM* powder is prepared as described in previous sections. A first set of cells is made depositing the ink using tape casting technique. The thermal treatment is composed by a heating ramp of 3°C/min until 1100°C, this temperature is maintained for 2 hours and then a cooling ramp of 3°C/min is used. There is not good adhesion of the ink over the pellet. To optimise the adhesion, a new composite ink is created. It is made of 75:25 in weight of *LSCM* and LSGM. This ink is used for the same reasons and with the same preparation method as described previously. Over the pellet on both sides, it is deposited a layer of the ink of 75wt%LSGM:25wt%*LSCM* and a layer of the ink made only of *LSCM*. The thermal treatment consists in a heating ramp of 1°C/min since 400°C, this temperature is maintained 10 minutes. After that a heating ramp of 3°C/min is used since 1200°C. This temperature is maintained for 2 hours. A cooling ramp of 3°C/min is used to reach room temperature. Adhesion is not found. So, a different thermal treatment is tempted. The stopping temperature is enhanced to 1300°C. Also, this time the ink adhesion required is not found. This is probably due to interactions between the ink layer and the electrolyte that reduce compatibility.

YSZ is thus preferred for electrochemical tests of *LSCM* ink and Ni@LSCM made by impregnation. Further studies are needed to understand the detrimental interaction between electrode and LSGM electrolyte.

5. *LSCM composite: Ni@LSCM*

In this section, Ni@LSCM sample is produced by impregnation method. The percentage of Ni is of 5wt%. In this way problems connected to Ni-based anodes, as the formation of carbon, should be reduced thanks to the interaction with the perovskite. The presence of Ni can enhance catalytic activity with both hydrogen and methane fuel.

5.1 Impregnation

The used nickel precursor is $Ni(NO_3)_2 \cdot 6H_2O$. The calculated amount of precursor necessary to obtain 5wt% of Ni metallic in the final sample was dissolved in water. Citric acid is added to the Ni solution. Citric acid amount is 1.9 times the concentration of metallic cations in solution. To assure the coordination of Ni particles on three sites of citric acid chain, the pH is selected to 7 using ammonium hydroxide to basify the solution. The 95wt% of *LSCM* is add. It is heated to evaporate all the water and a wet gel is formed. After that the temperature is raised since 350°C. At this temperature there is the gel spontaneous combustion. The powder is formed, and a thermal treatment is needed. The powder is heated 3°C/min since 850°C. This temperature is maintained for 2 hours and it is cooled to room temperature using a ramp of 3°C/min. Also, in this case the heating rate has been optimized.

Impregnation permits the creation of an intense interaction between Ni and *LSCM* powder. In fact, in this case Ni can be deposited over single *LSCM* grains independently by their dimension. Moreover, in contrast to infiltration, nickel dispersion is not dependent on the capability of solution to percolate between *LSCM* grains.

5.1.1 X-Ray Diffraction (XRD)

The used instrumentation was already described. The measure takes place using 0.03°/step at a counting time of 10 s/step in the range between 20° and 70°, at room temperature. The phase is identified by the search and match method using JCPDS database. The XRD patterns of *LSCM* and of Ni@LSCM are reported in *Figure 43.* It is possible to see the characteristic peaks of *LSCM* in both the samples. The presence of NiO is not evidently found. It is caused by the low amount of nickel that has been impregnated. Peaks between 25-30° are due to La_2CrO_6 phase and are evident in

Ni@LSCM sample. This phase disappeared if reducing atmosphere is used. Its presence is revealed only in the Ni@LSCM sample because of the higher temperature of calcination utilised that favours the formation of this type of impurities.

The impregnated sample has a higher crystallinity because of the additional thermal treatment at 850°C. The average dimension of crystallites is 20 nm, using Scherrer equation. They have a higher dimension than the crystallite of non-impregnated perovskite sample (15 nm).

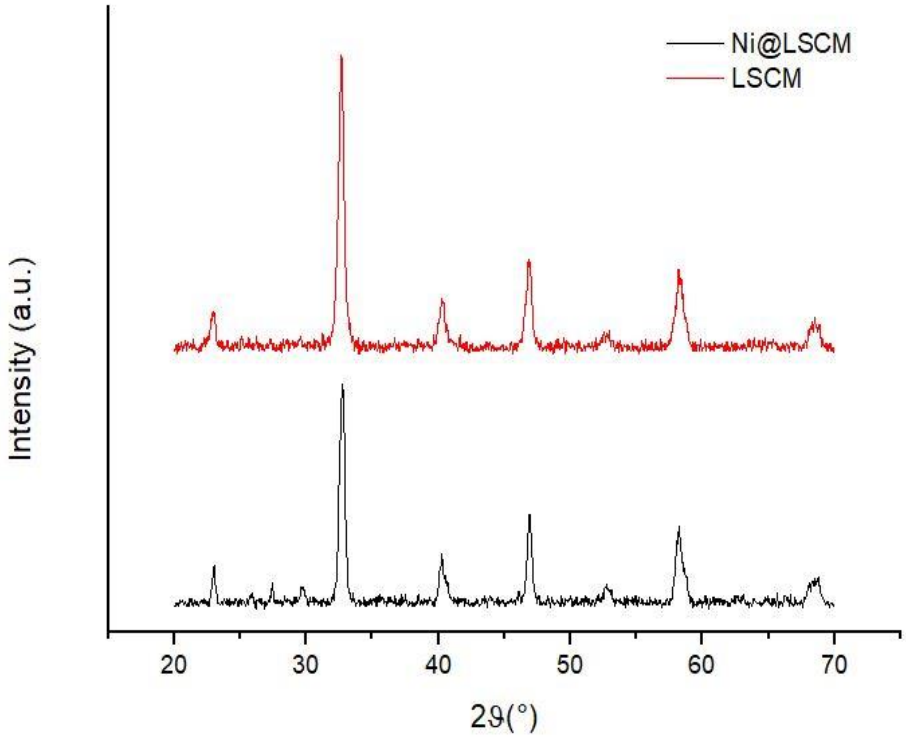

Figure 43. XRD pattern of LSCM (red) and Ni@LSCM (black) samples.

5.1.2 Temperature Programmed Reduction (TPR)

H_2-Temperature Programmed Reduction of the powder has been made. The data are collected as already illustrated. In *Figure 44*, the curve of reduction of Ni@LSCM is reported and compared with the one of *LSCM*. In the case of Ni@LSCM sample, it is possible to see an intense peak at 470°C with a shoulder. Two gaussian peaks can be deconvoluted. The peak centred at 482°C can be correlated to the reduction of NiO to Ni ($Ni^{2+} \rightarrow Ni^0$). Meanwhile, the peak at 457°C is related to this reaction $Mn^{4+} \rightarrow Mn^{3+}$. The experimental consumption of hydrogen is of 1.06 10^{-4} mol. This value is in good agreement with the estimated one calculated considering the complete reduction of Ni(II) to Ni(0) and of Mn(IV) to Mn(III). The theoretical consumption of Ni is 8.92

10^{-5} mol and the one of Mn is 4.40 10^{-5} mol. The total theoretical consumption is the sum of 1.33 10^{-4} mol. Another peak of lower intensity at 350°C can be found. It is due to the reduction of the La_2CrO_6 phase previous seen in XRD pattern.

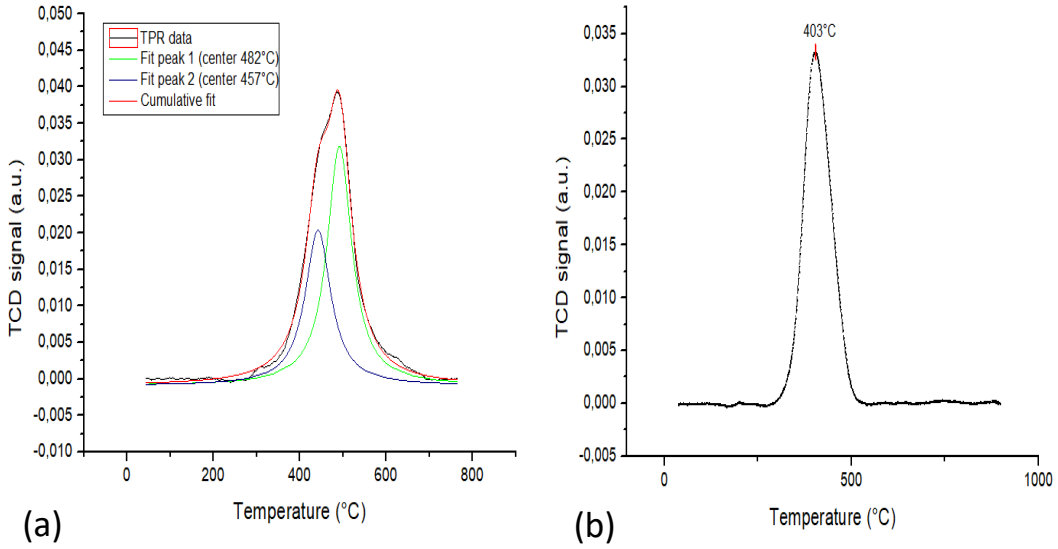

Figure 44. (a)TPR curve for Ni@LSCM powder. TPR data are deconvoluted and two gaussian peaks centred at 482°C and 457°C can be found. (b) TPR curve for LSCM powder. A single gaussian peak at 403°C is revealed.

5.1.3 Brunauer – Emmett – Teller Surface Area (BET)

The surface area determination of Ni@LSCM sample is performed using ASAP2020 Plus. The surface area measured is of 5.7±0.1 m^2/g, less than the one for the sample without impregnation. This can be due to the higher calcination temperature required for the Ni@LSCM with respect to *LSCM* sample. In fact, Ni@LSCM was calcinated at 850°C to have the formation of NiO particles, instead starting powder was calcinated at 700°C.

The isotherm linear plot for Ni@LSCM sample is reported in *Figure 45*.

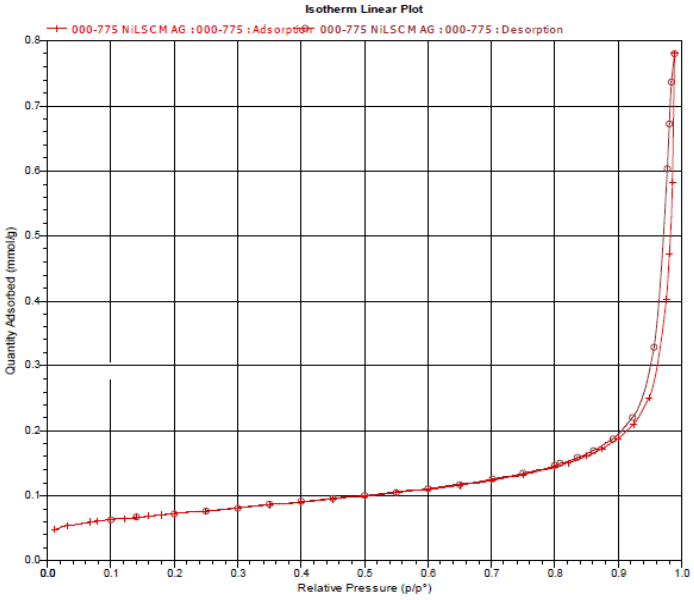

Figure 45. Ni@LSCM isotherm linear plot.

In nitrogen adsorption analysis six types of adsorption curves can be found, using IUPAC classification. The case of our interest can be correlated to a type II behaviour, typical of macroporous structures with stronger interactions with the adsorbate .[41] It can be noted a hysteresis cycle between adsorption and desorption signal. The hysteresis loop can be related to H3 type in IUPAC classification. It represents a solid formed by aggregates or agglomerates of particles forming slit-shaped pores with nonuniform size or shape.[41]So, Ni@LSCM sample has the same behaviour of *LSCM*.

In *Figure 46*, it is possible to see pore width distribution, calculated by BJH method.[42] There is a unique peak which indicates an high volume percentage of pores of 2-3nm-width. This can be associated to superficial porosity, in fact the estimated average pore width is of 24nm. Pores with a major dimension are still present but there is not a second peak at 30 nm as in the case of pure *LSCM* sample. This is due to nickel preferential deposition sites. In fact, pores of 30 nm-width are the sites in which nickel nucleation is particularly successful. This can be a problem because the capability of gases to percolate could be reduced. Maybe a lower percentage of nickel is required to maintain also pores of higher dimension and obtain an adequate dispersion.

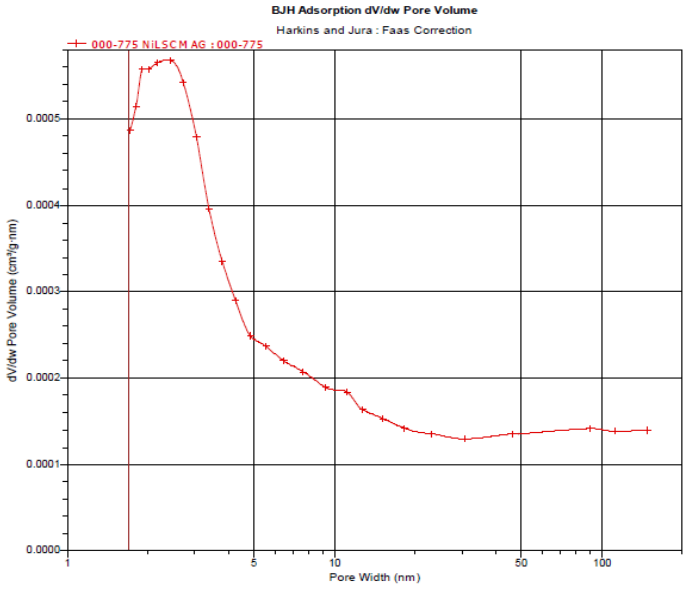

Figure 46. Ni@LSCM pore width distribution.

5.1.4 Scanned Electron Microscopy (SEM)/ Energy Dispersed X-ray Analysis (EDX)

SEM images of Ni@LSCM are reported in *Figure 47*. The morphology is comparable with the correspondent sample of *LSCM*; moreover, the compact structure of Ni@LSCM sample can be observed.

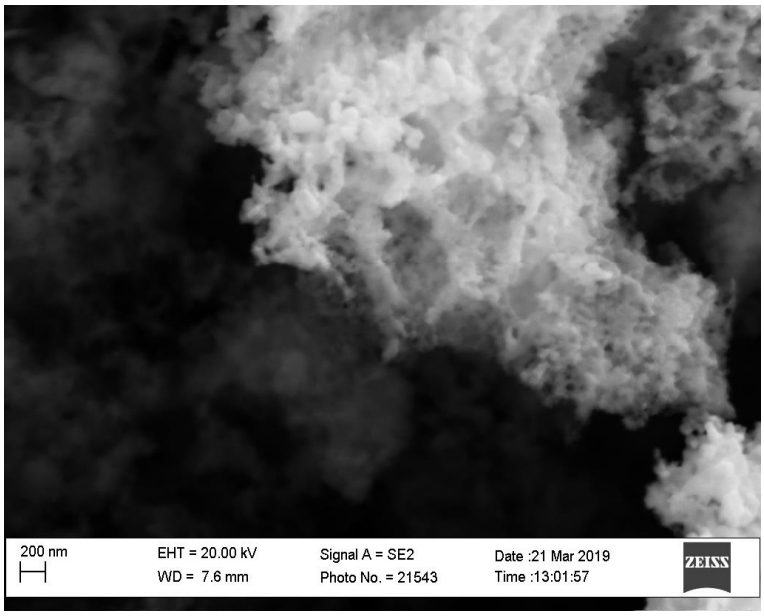

Figure 47. SEM image taken with at 20.00kV and 25k of magnification for Ni@LSCM sample.

EDX atomic compositions are compared with *LSCM* and nominal ones in *Table 7*.

Table 7. EDX cation concentration (%) for Ni@LSCM and LSCM2 samples and theoretical values obtained for the weighted amounts.

	LSCM2	**LSCM Theoretical value**	**Ni@LSCM**	**Ni@LSCM Theoretical value**
Element	*Concentration (%)*	*Concentration (%)*	*Concentration (%)*	*Concentration (%)*
La	29.9	37.5	35.2	35.7
Sr	23.9	12.5	16.2	11.9
Cr	20.5	25.0	14.9	23.8
Mn	25.8	25.0	29.0	23.8
Ni			3.8	4.8
Cr/Mn	0.79	1.00	0.51	1.00
Sr/La	0.80	0.34	0.46	0.34

Comparing the calculated values of cations concentration in the case of the starting *LSCM* powder and in the case of the Ni@LSCM, it can be noted that there is a higher percentage of manganese cations in the impregnated sample. This fact can be connected to a nickel attitude to interact with this cation. Lanthanum concentration is in good agreement with the theoretical value for Ni@LSCM sample, instead in LSCM2 its concentration is lower. In Ni@LSCM, chromium concentration is lower than the theoretical value like in *LSCM* sample. Strontium percentage in Ni@LSCM is elevated as in the case of LSCM2, even if it is less evident in the impregnated sample. The percentage of nickel that is revealed is less than the one theoretically impregnated.

5.1.5 X-ray Photoelectron Spectroscopy (XPS)

XPS gives important information about the quantitative presence of each element on the surface of the sample. Moreover, photoelectron lines position can be discussed.

To analyse Ni impregnated sample, it is necessary to understand the adequate X-ray source. Comparing the binding energy of photoelectron lines for each element with the energy position of Auger lines that depends on the source utilised, it is possible to avoid eventual overlaps. If K-α line of Al is used as X-ray source, an overlap between Auger line due to La and Ni most intense peaks is evident. To avoid this, K-α line of Mg is used. As before, for each element, it is selected a region in binding energy in which the most intense photoelectron peaks usually stay. The spectrum is taken utilising low resolution acquisition setup, associated to a passing energy of 117eV.

Only carbon impurities can be revealed and associated to superficial contamination of the sample. For Cr, O, Mn, Sr the most intense peaks are revealed, and their area is related to their concentration. In the case of Ni, its most intense peak at 853eV, connected to Ni^{2+} $2p_{3/2}$ orbital is not visible. This is due to La peaks overlap. Even if Ni second most intense peak is chosen as the peak of interest to determine its concentration, it is not visible because of the low percentage of Ni utilised during impregnation. So, Ni concentration is not calculated, and La concentration will be overestimated due to Ni peak overlap.

XPS reveals superficial cation concentration for Ni@LSCM prepared by impregnation of LSCM2 sample. Element concentration is estimated utilising area evaluation of the most intense photoelectric peaks. Baseline is calculated by the software utilising the Shirley method, after operator evaluation of peak extremities.

XPS cations concentration for LSCM2 sample and Ni@LSCM are compared in *Table 8*. Lanthanum concentration in Ni@LSCM sample is higher than the theoretical value, this is evident also in LSCM2. Moreover, lanthanum concentration is overestimated because its XPS peaks overlap the ones of nickel. For this reason, nickel percentage is not reported. Chromium concentration results lower than the theoretical value as in LSCM2 sample. Instead strontium concentration is higher in Ni@LSCM. In Ni@LSCM, manganese superficial concentration is lower than the theoretical one in opposition to what happen in LSCM2. This indicates that the presence of nickel modifies manganese distribution.

Table 8. XPS cation concentration (%) for Ni@LSCM and LSCM2 samples and theoretical values obtained for the weighted amounts.

	LSCM2	**LSCM Theoretical value**	**Ni@LSCM**	**Ni@LSCM Theoretical value**
Element	*Concentration (%)*	*Concentration (%)*	*Concentration (%)*	*Concentration (%)*
La	43.6	37.5	39.5	35.7
Sr	12.2	12.5	19.6	11.9
Cr	16.8	25.0	18.6	23.8
Mn	27.4	25.0	22.2	23.8
Ni			-	4.8
Cr/Mn	0.61	1.00	0.84	1.00
Sr/La	0.28	0.34	0.50	0.34

These data can be confronted with the ones of EDX. Chromium concentration is higher in superficial layer, analysed by XPS. Manganese presents the opposite behaviour, demonstrating its interaction with nickel and movement to deeper layers. Strontium concentration results more elevated in superficial layers, indicating its possible segregation. Lanthanum percentage is more elevated in superficial layers, instead EDX revealed that its concentration is in good agreement with theoretical values in the bulk.

By analysing Cr/Mn and Sr/La ratios, it can be noted that chromium concentration is lower than the theoretical value. In Ni@LSCM sample, chromium concentration is higher in superficial layer as demonstrated by an elevated Cr/Mn ratio revealed by XPS. This fact indicates that nickel interacts with manganese and prefers to move to deeper layers. This implies that nickel percentage on superficial layer would be not elevated as expected, lowering possible catalytic advantages related to its presence. This fact is correlated to higher Mn^{4+} reduction temperature if nickel is impregnated. Moreover, strontium concentration is higher in relation to lanthanum in the case of Ni@LSCM sample. This indicates possible strontium segregation not only in superficial layer, analysed by XPS but also deeper as demonstrated by EDX. This is a detrimental factor for future electrode performance because strontium oxide and carbonates are not conductive species.

6. *Cell study of Ni@LSCM*

Ni@LSCM is now studied in electrochemical cell tests. An ink has been produced from the powder and it has been deposited by tape casting over electrolyte pellets. Electrochemical Impedance Spectroscopy has been utilised to analyse electrode proprieties. In particular, the same experimental apparatus and methodology as before have been selected. Both hydrogen and methane have been inlet as fuel. Performance of Ni@LSCM sample are reported in next sections and are confronted with the ones of *LSCM*.

6.1 Ni@LSCM/YSZ device

The electrolyte chosen is YSZ. In this way, it is possible to compare impregnated anode performance with the one of the cells previously tested. An ink has been prepared made by Ni@LSCM powder and YSZ (75wt%:25wt%). This ink has been selected because has been previously seen that using this composition, the adhesion problems are reduced. Ink has been deposited on both sides of YSZ pellets by tape casting. After that, a second layer made by only Ni@LSCM ink has been deposited. As previously seen for *LSCM*, the second layer has an optimal adhesion over the first one. The cell has been thermally treated. A heating ramp of 1°C/min since 400°C has been chosen, this temperature has been maintained 10 minutes. After that a heating ramp of 3°C/min is used since 1300°C. This temperature is maintained for 2 hours. Room temperature is achieved using a cooling ramp of 3°C/min.

The electrical contact is made using gold paste as electron collector. The paste is deposited over the ink on both sides using a paint brush, following the procedure developed and explained in Chapter 4. After deposition, every cell is thermally treated to stabilise electrode layer. The temperature is raised 2°C/min since 800°C and it is maintained for 1 hour. The next cooling ramp is of 2°C/min since room temperature.

6.2 Hydrogen fuel

Impedance spectrum has been taken using a gas flux of 200sccm with 10% H_2 in Ar. Electrochemical tests has been performed at 800°C, 775°C,745°C,715°C, 690°C and 660°C. In *Figure 48*, the Nyquist plots obtained at the mentioned temperatures, are compared.

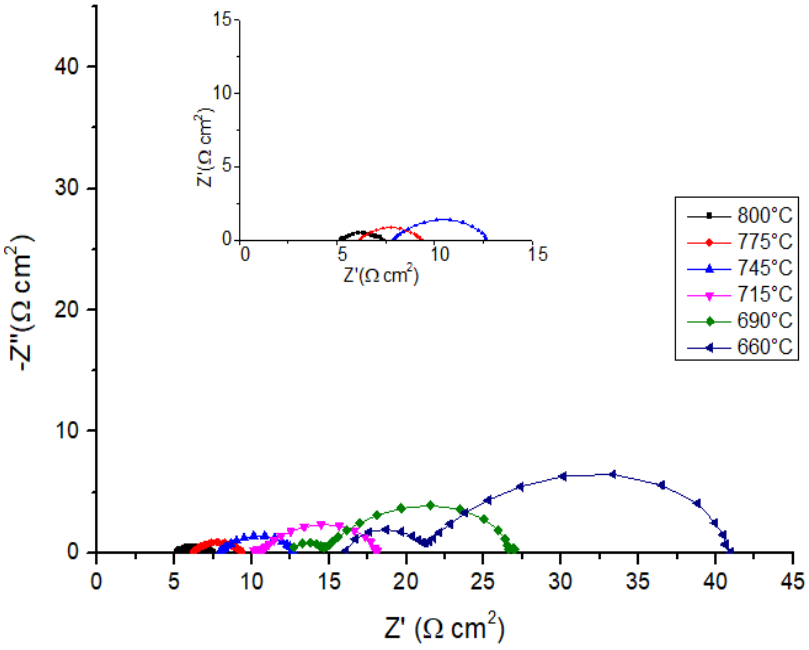

Figure 48.Nyquist plots taken at different temperatures, using 10% of H2 as fuel and gold paste as electron collector. In the inset, enlargement of the data collected at higher temperatures of 800°C, 775°C and 745°C.

The impedance behaviour can be described as before by a Rs, polarisation resistance due to electrolyte in series with an inductance, L, and two parallel circuits composed by a resistance R and a CPE, constant phase element (see model circuit in *Figure 34).*

R_s, the ohmic resistance associated with the one of electrolyte is lower at higher temperature and increases at lower temperature.

The frequencies associated with the two processes described by R-CPE circuit are of the same order of magnitude of the precedent case. There is a process at high frequencies between 10^2 -10 Hz and one at low frequencies, 10^{-1} Hz. The first process is connected to gas-solid interaction as adsorption/desorption on surface and the second one to gas diffusion. At high temperature, the process at higher frequency is the rate determining step instead of the cases in which *LSCM* is the electrode. In fact,

in this case the resistance associated to the high frequency process has a higher value than the one associated to low frequency process.

It is possible to associate at each measure an ASR value that describes the sum of the resistive processes that take place, normalised by the electrode area. These values are listed in *Table 9*. ASR values for Ni@LSCM sample are lower than the ones calculated for *LSCM* electrode at the same temperature. This fact demonstrates that the presence of nickel improves the electrocatalytic proprieties of *LSCM* electrode. This is due to an enhancement in electrical conductivity and catalytic activity.

Table 9. ASR values associated to the temperature of measurement.

T(°C)	ASR ($\Omega \cdot cm^2$)
800	1.4
775	1.7
745	1.9
715	2.3
690	2.8
660	3.2

The logarithm of ASR can be plotted in function of 1/T, with T expressed in Kelvin. By Arrhenius formula, it can be calculated the activation energy. The logarithm of ASR and 1/T are connected by a linear relation, see *Figure 49.* This result indicates that there is a single activated process. The calculated activation energy, Ea is 1.09±0.01eV. Ea value for *LSCM* electrode is higher than the one for Ni@LSCM sample. This fact is consistent with the enhancement of the electrode performance due to the impregnation with nickel. As expected, nickel presence enhances catalytic activity utilising hydrogen as fuel. Nickel impregnation can have a positive effect also increasing electronic conduction (Ni is a good conductor). In this way, the electrode mixed electronic and ionic conductivity is enhanced, lowering TPB problems. Also, the synergic effect due to nickel interaction with manganese, suggested by the characterisation techniques (XPS vs EDX), can positively affect electrode performance.

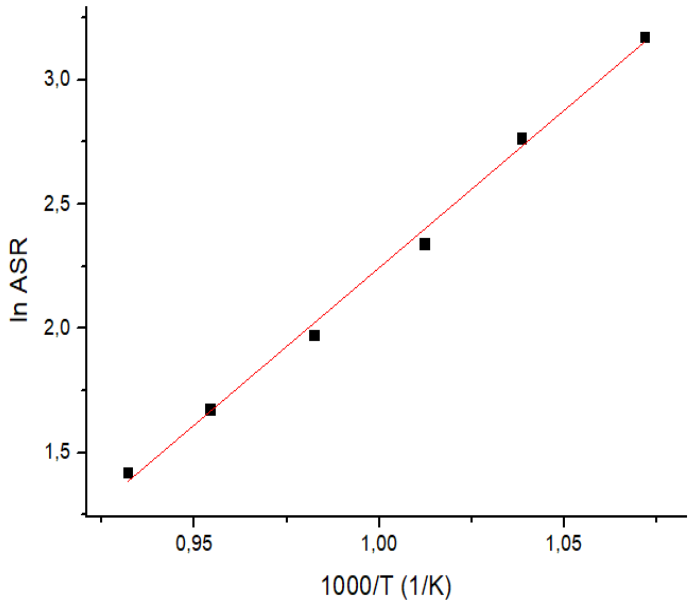

Figure 49. Linear plot of ln ASR in function of 1000/T, with T expressed in Kelvin.

Different hydrogen concentrations have been utilised. A flux of 200sccm is injected in the experimental setup. At 800°C, a flux of 5%, 10% and 20% of H_2 in Ar has been used. In *Figure 50*, different impedance spectra obtained at different hydrogen percentage, are compared.

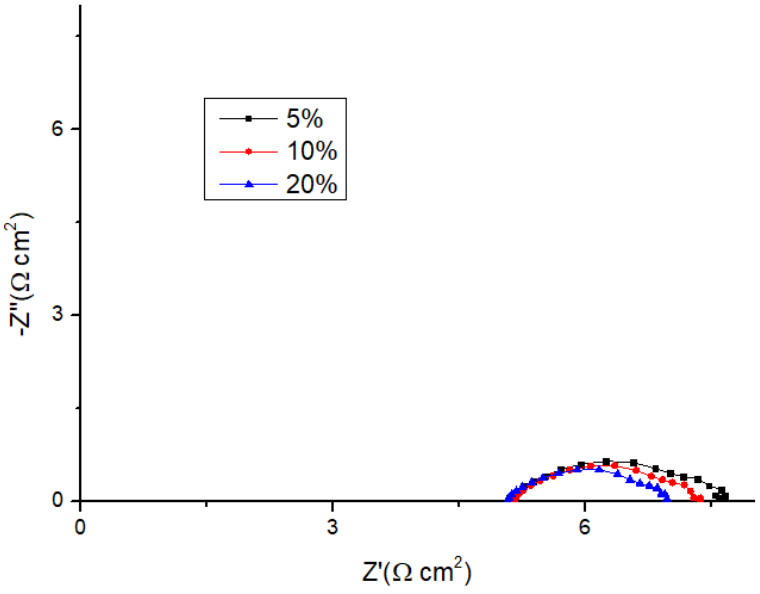

Figure 50. Nyquist plots taken at 800°C, using 5%,10% and 20% of H_2in Ar as fuel and gold paste as electron collector.

The model circuit mentioned in the previous sections, suggests the presence of two processes, one at higher frequencies (10Hz) and one at lower ones (10^{-1}Hz). The first

process is connected with the electrochemical performance of the cell and it is independent by gas flux. Instead, the low-frequencies process is due to gas diffusion.

6.3 Methane fuel

Impedance spectrum has been taken using a gas flux of 200sccm and gold paste as electron collector. To reach the temperature of analysis, a gas flux composed by 10% H_2 in Ar is selected. Methane is then inlet as fuel, in particular a 10% of CH_4 in Ar is utilised. Impedance analysis has been performed at 815°C, 790°C, 760°C, 730°C, 700°C and 670°C. In *Figure 51*, the Nyquist plots obtained at the mentioned temperatures are compared.

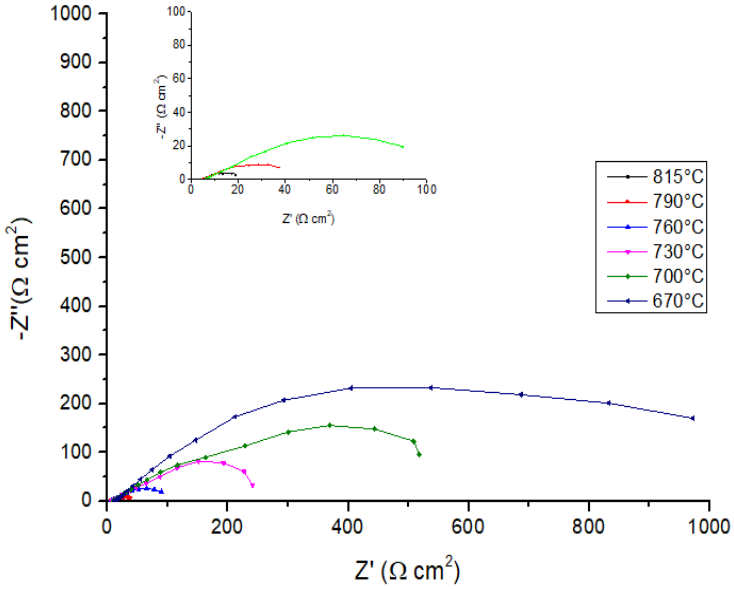

Figure 51. Nyquist plots taken using as fuel methane (10% CH_4 in Ar) at different temperatures. In the inset, enlargement of the data collected at higher temperatures of 815°C, 790°C and 760°C.

The impedance behaviour can be described by the model circuit in *Figure 34*. There are two processes: one characterized by frequencies between 1-10^{-1}Hz and the second by a frequency of 10^2Hz. It can be noted that the total polarisation resistance increases significantly when methane is used instead of hydrogen. The first process at high frequencies can be related to gas-solid interaction as adsorption, dissociation, desorption or to surface diffusion of the adsorbed species, as mentioned before. The low frequency process is usually due to gas phase diffusion.

It is possible to associate at each measure an ASR value that describes the sum of the resistive processes, normalised by the electrode area. These values are listed in *Table 10.* Nickel impregnation permits to obtain a lower ASR value at elevated temperature. This demonstrates that the presence of nickel improves electrocatalytic proprieties of the exanimated electrode. At low temperature, the ASR values are higher than for pure *LSCM* sample. This can be due to partial poisoning of nickel due to the utilisation of methane as fuel.

Table 10. ASR values associated to the temperature of measurement.

T(°C)	ASR ($\Omega \cdot cm^2$)
815	12.9
790	26.6
760	63.9
730	184.4
700	272.1
670	553.8

The logarithm of ASR can be plotted in function of 1/T, with T expressed in Kelvin. A linear behaviour, correlated to a single activated process independent by temperature, can be observed (see *Figure 52).* Calculated activation energy is: Ea=2.44±0.01eV. In this case, the activation energy of Ni@LSCM electrode is higher than the one measured for *LSCM* electrode.

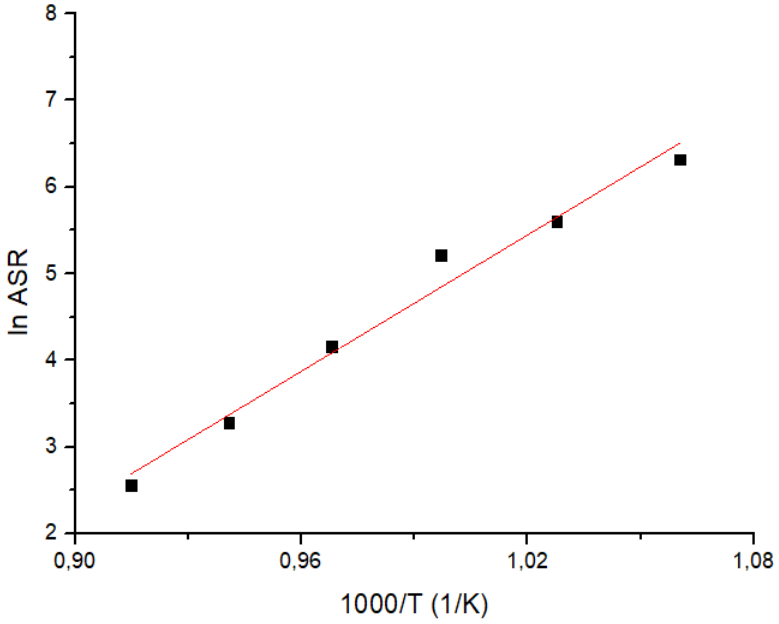

Figure 52. Linear plot of ln ASR in function of 1000/T, with T expressed in Kelvin.

Utilising methane as fuel, nickel impregnation permits to achieve a performance enhancement due to its catalytic activity toward methane oxidation. This is demonstrated by a lowering in ASR value in relation to pure *LSCM* case. However, the advantages due to nickel are lost at lower temperature. In fact, in this condition, the poisoning by carbon deposition (connected with methane cracking reaction) becomes relevant. The electrode performance is lower than the one of *LSCM* and this is attributed to the interaction between nickel and manganese. TPR analysis demonstrates manganese stabilisation: higher temperature of reduction of Mn^{4+} specie than in the case of *LSCM*. Moreover, from EDX and XPS, it is demonstrated a manganese migration to deeper layers due to nickel interaction. The migration of Ni toward bulk and the stabilization of the Mn(IV) species decrease the performance both lowering the catalytic activity and the conductivity (ionic and electronic). The decreasing ionic conductivity is evident when nickel is poisoned, and its catalytic activity and efficient manganese interaction are lost. To enhance the electrode proprieties and performance, the addition of an ionic conductor could be useful. Moreover, from BJH data it has been revealed nickel attitude to occupy pores of bigger dimension where methane molecule could easily interact with *LSCM*. This fact further reduces electrode performance.

Conclusions

The proposal of this thesis is the study of an innovative anode material, that can be implemented on a Solid Oxide Fuel Cell system. This choice is due to the enhancement on researches aimed at reducing pollutant emissions and improving an environmentally friendly way to storage and convert energy. In this context, the study of SOFCs, or in general fuel cells has become an interesting topic. In fact, these devices permit the direct conversion of chemical energy of fuels in electrical energy with low pollutants emission. Moreover, Solid Oxide Fuel Cells work at elevated temperature and this permits the advantage of a certain fuel flexibility and an increased efficiency. The necessity of electrodes based on noble metals is drastically reduced and this leads to a decrease of materials costs. Fuel flexibility permits to avoid hydrogen as fuel at the anode side. Hydrogen is difficult to produce, and it can lead to transport problems. So, the possibility to use hydrocarbons, like methane, has to be explored. In fact, the presence of efficient ways of transport for these gases is an advantage for future commercialisation.

This work focuses on the development of an anode material. An efficient anode has to possess several proprieties like: stability in reducing environment at elevated temperatures, mixed ionic and electronic conductivity to enhance the TPBs and the performance, catalytic activity to fuel oxidation and a porous morphology to allow gas diffusion. The state-of-the-art material is a cermet based on Ni-YSZ. Even if, it possesses good proprieties and performance, the presence of 40% of Ni leads to several disadvantages. In particular, the poising effects due to hydrocarbons utilisation as fuel reduces the possibility of avoiding hydrogen. So, new materials have to be investigated. Perovskites demonstrates an elevated tunability and implementation of interesting proprieties by doping. $LaCrO_3$ perovskite is characterized by numerous advantages that already permits its utilisation as interconnect in SOFCs. In fact, it is stable in both reducing and oxidising atmosphere at elevated temperatures and possess an elevated electronic conductivity in both the environments. By doping on A and B sites of the perovskite structure, it is possible to improve or create new proprieties that permits its utilisation as anodic material. On A-site, Sr has been inserted. This choice is due to the fact that an element with a lower oxidation number (aliovalent doping) should lead to the formation of oxygen vacancies and enhanced the ionic conductivity.

Moreover, it permits the formation and stabilisation of the redox couple due to the doping of Mn on B-site. Mn presence leads to an increment of electronic conductivity and catalytic proprieties. $La_{0.75}Sr_{0.25}Cr_{0.5}Mn_{0.5}O_3$ (*LSCM*) is the material studied in this project and it is fully characterised by different techniques. Its electrochemical proprieties are investigated using both hydrogen and methane as fuel. To improve the electrochemical characteristics of this material, impregnation of nickel has been tempted. Nickel has been chosen because it can enhance electrochemical properties, catalytic activity and electronic conductivity. To avoid its detrimental effects on the cell, I decided to impregnate with a low amount (5wt% of Ni on *LSCM*) in this way I expect a good interaction with the perovskite and thus less sintering and lower attitude toward C-poisoning. Also, this material has been fully characterised, and its electrochemical proprieties have been tested using both hydrogen and methane as fuel.

Materials proprieties

Material synthesis has been performed through *Marcilly* method. This implies the use of metallic precursors dissolved in water or nitric acid and citric acid as complexing agent. The adequate pH of 7-8 has been reached utilising ammonium hydroxide, this permits to reach the third constant of dissociation of citric acid. By self-combustion of the wet-gel formed and successive calcination, the powder of interest has been produced.

To characterise *LSCM* and Ni@LSCM samples, several techniques have been used.

Perovskite peaks have been found into diffraction pattern made by XRD. The quantity of nickel impregnated is lower than the minimum value revealed by the instrumentation. So, nickel presence has not been found in diffraction pattern, as expected.

A TPR analysis has been done to understand the processes of reduction that take place at different temperatures. *LSCM* sample presents a TPR curve characterised by a single peak at 403°C. The temperature at which the reduction process takes place and the hydrogen consumption reveal that the reduction of Mn^{4+} to Mn^{3+} is the process of interest. This demonstrates the presence of the redox couple Mn^{4+}/Mn^{3+}, as expected. Instead TPR curve for Ni@LSCM sample is composed by two peaks associated to two reduction processes. The process at 457°C is connected with Mn^{4+}/Mn^{3+} reduction as in the case of pure *LSCM*. The second peak at 482°C is due to NiO reduction to Ni.

This is related to the fact that the calcination of Ni@LSCM sample has been performed in air, leading to the formation of NiO that during a temperature programmed reduction reduces to Ni. The interesting fact is that the presence of nickel stabilises Mn^{4+} species, enhancing the temperature at which manganese reduction takes place.

A morphological study carried out with SEM confirms that *LSCM* and Ni@LSCM samples possess a similar structure not influenced by nickel impregnation.

Surface areas have been calculated utilising BET method. This analysis reveals that *LSCM* powder calcinated at lower temperature (700°C) presents a surface area of 13.0±0.1 m^2/g. This value is higher than 5.7±0.1 m^2/g, calculated for Ni@LSCM sample that has been calcinated at 850°C. These surface areas are in good agreement with data found in literature for perovskite samples. Even if, the surface area is not elevated in perovskites their capability to reach significant catalytic proprieties and a mixed ionic and electronic conductivity makes them interesting potential electrode materials. By BJH approximation, it is also possible to calculate the average porosity width that for *LSCM* is 27.1 nm, instead for Ni@LSCM is 24 nm. From pores distribution, it can be revealed that pores population of 30nm-width decreases in Ni@LSCM sample. This is connected to NiO agglomeration inside porosity of higher dimensions, lowering gas diffusivity during electrochemical tests.

X-Ray Photoelectron Spectroscopy and Energy Dispersion X-Ray analysis have been used to study the composition of the powders and to evaluate eventual segregation processes. Nickel presence has been revealed only by EDX and it is in good agreement with the theoretical percentage. In XPS the overlap of La^{3+} $3d_{5/2}$ peaks over the region where Ni^{2+} $2p_{3/2}$, nickel most intense contribution is situated does not make possible nickel percentage evaluation. Comparing XPS and EDX data for the determination of other cations percentage it can be noted several information. Chromium concentration is lower than the theoretical one for both the samples. This behaviour is proved by both XPS and EDX techniques. This can be related to the fact that chromium is present more in deep layers of the perovskite or that a consistent chromium percentage has escaped by the structures in a volatile form during synthesis. Moreover, manganese concentration is lower in superficial layer for Ni@LSCM sample, indicating that these cations interact more with nickel. This fact and an enhanced temperature for Mn^{4+}reduction demonstrates that nickel strongly interacts with manganese. Moreover, manganese moves away from surface, indicating that also superficial nickel presence

is lower than the one expected. Finally, strontium concentration is higher in superficial layer. Strontium segregation and nickel interaction with manganese in Ni@LSCM sample can reduce electrocatalytic activity of the impregnated sample.

Cell construction

Electrolyte supported cells have been produced, starting from an electrolyte pellet and depositing by tape casting the electrode material. The electrolyte choice has been performed starting from a compatibility test that leads to identify the adequate material. Tests demonstrated that YSZ is a possible choice. After that, an ink based on the electrode powder has been realized. Soot was also added to this ink to obtain an elevated porosity on the final electrode while the adequate ink viscosity is defined by two α-terpineol based polymers. The ink composition has been investigated and optimized to improve adhesion on the electrolyte pellets. By several tests, the optimal method consists on the deposition of an ink composed by 75wt% of *LSCM* and 25wt % of YSZ as the first layer and a second layer of pure *LSCM* ink. The electrode has been then calcined since 1300°C. The first layer demonstrates elevated adhesion on YSZ pellets thanks to its composition and allows improving the adhesion of the *LSCM* pure layer.

The comparison of the obtained adhesion suggested the choice of YSZ (Yttria Stabilized Zirconia) instead of LSGM (a Sr,Mg-doped lanthanum manganite) as electrolyte for successive electrochemical tests.

Moreover, several attempts have been made to optimise electron collector adhesion over the electrode. Gold paste deposited by tape casting demonstrated a low adhesion due to the fact that a thick layer of gold has been deposited. So, a nickel paste has been deposited using a paint brush, in this case electrochemical performance demonstrated the presence of an elevated ASR and two different activation energies depending on temperature range. Also, the utilisation of a gold paste added with 5wt% of soot has the same effects. Only a gold paste deposited by a paint brush demonstrates a reduction in ASR values. It is probable that nickel and gold paste added with soot do not possess an adequate electronic conductivity: the use of soot leads to an enhancement into electron collector layer porosity and theoretically this can lead to a reduction of the resistance connected to gas diffusion process. Unfortunately, gold paste and soot tend to separate after mixing resulting in the deposition of a not-continuous and not-

homogeneous layer. All the electrochemical tests have been performed using brash deposited gold paste as electron collector.

Electrochemical proprieties

Electrochemical proprieties have been analysed utilising EIS technique. At different temperatures, between 830°C and 660°C, the impedance behaviour has been studied. Both *LSCM* and Ni@LSCM electrodes and hydrogen and methane fuels have been investigated and electrochemical response has been compared.

Nickel impregnation enhanced the performance of the electrode both in hydrogen and methane. In hydrogen, ASR values are lower both utilising *LSCM* and Ni@LSCM sample. This is due to the fact that hydrogen oxidation is easier than hydrocarbons oxidation. Nickel impregnation increased the performance enhancing electronic conductivity and catalytic proprieties. The activation energy calculated by Arrhenius formula is of 1.41±0.01eV for *LSCM* and of 1.09±0.01eV for Ni@LSCM sample. Indicating that nickel presence reduces the energy of activation and increases electrode performance. Instead, if methane is utilised as fuel, ASR values are reduced at high temperature by nickel impregnation. At lower temperature the effect is no more valid. Moreover, the activation energy for *LSCM* sample is of 1.3±0.1eV and for Ni@LSCM is of 2.44 ±0.01eV. This suggests that, at lower temperature, the electrode can be poisoned by carbon formation. Even if a low amount of nickel has been impregnated the electrode performance decreases at low temperature. Moreover, nickel interaction with manganese could lead to a lowering of ionic conductivity after nickel poisoning. The total activation energy enhancement is caused by this factor.

The impedance behaviour for all the cases mentioned above can be described by a model circuit. This is composed by a resistance in series with an inductance and with two circuits composed by a resistance and a constant phase element in parallel. The first resistance is due to electrolyte. It increases at lower temperature and it is independent by gas flux. The two circuits composed by a resistance in parallel with a CPE describe the electrochemical behaviour of electrodes that in a Nyquist plot corresponds to two depressed arcs. By the phase region in Bode plot at which these processes take place, they can be justified. Processes that take place at 10-10^4 Hz are associated to a gas-solid interaction as adsorption, dissociation, desorption or to surface diffusion of the adsorbed species. An arc with frequencies below 1Hz is usually

related to gas phase diffusion; whose characteristic frequency is between 1-10Hz. Another explanation to low-frequency process is “chemical capacitance”. This contribution is due to the variation in the oxygen non-stoichiometry of the ceramic electrode. It represents the capability of the sample to store chemical energy through oxygen vacancies upon changes in the local oxygen chemical potential. In *LSCM* electrode, it is usually associated with gas diffusion correlated to electrode microstructure.

Future prospective

LSCM and Ni@LSCM samples have demonstrated interesting characteristics as anodic material in both hydrogen and methane atmosphere. An important future step would be the production of a new material made by infiltration of nickel on *LSCM*. In this way, it would be possible to suggest in which way nickel can enhance more catalytic proprieties. Moreover, the nanocomposte electrode performance can be enhanced by depositing a specie active in methane oxidation.

Other hydrocarbons can be tested as fuel. Performance can be confronted to better understand the processes that take place modifying electrode and fuel composition. Moreover, TPD or TPO techniques can give further information about the oxygen mobility inside the electrode at working temperature.

Another topic can be the optimisation of ink adhesion over LSGM pellets. Different multilayer composition can be tested. A possibility is the use of a first layer composed by 75wt % LSGM and 25wt % *LSCM* that can have an elevated adhesion on LSGM pellets. It will be followed by other layers containing a higher amount of *LSCM* and reducing the quantity of LSGM to gradually enhance superficial layer adhesion.

Finally, *LSCM* electrode can be tested in oxidising environment. In this way the possibility to utilise *LSCM* in a symmetric and reversible cell can be exploited. Also, nickel impregnated, and infiltrated samples would be tested in these conditions.

Bibliography

1. Edition, S. & Virginia, W. Fuel cell handbook. *Choice Rev. Online* **26**, 26-6292-26–6292 (2013).
2. Moseley, P. T. *Fuel Cell Systems Explained*. *Journal of Power Sources* **93**, (2001).
3. Wang, Y., Chen, K. S., Mishler, J., Cho, S. C. & Adroher, X. C. A review of polymer electrolyte membrane fuel cells: Technology, applications, and needs on fundamental research. *Appl. Energy* **88**, 981–1007 (2011).
4. Kamarudin, S. K., Achmad, F. & Daud, W. R. W. Overview on the application of direct methanol fuel cell (DMFC) for portable electronic devices. *Int. J. Hydrogen Energy* **34**, 6902–6916 (2009).
5. Merle, G., Wessling, M. & Nijmeijer, K. Anion exchange membranes for alkaline fuel cells: A review. *J. Memb. Sci.* **377**, 1–35 (2011).
6. Sammes, N., Bove, R. & Stahl, K. Phosphoric acid fuel cells: Fundamentals and applications. *Curr. Opin. Solid State Mater. Sci.* **8**, 372–378 (2004).
7. Abdalla, A. M. *et al.* Nanomaterials for solid oxide fuel cells: A review. *Renew. Sustain. Energy Rev.* **82**, 353–368 (2018).
8. McIntosh, S. & Gorte, R. J. Direct Hydrocarbon Solid Oxide Fuel Cells. *Chem. Rev.* **104**, 4845–4866 (2004).
9. Minh, N. Q. Solid oxide fuel cell technology - Features and applications. *Solid State Ionics* **174**, 271–277 (2004).
10. Orera, A. & Slater, P. R. New chemical systems for solid oxide fuel cells. *Chem. Mater.* **22**, 675–690 (2010).
11. Shaikh, S. P. S., Muchtar, A. & Somalu, M. R. A review on the selection of anode materials for solid-oxide fuel cells. *Renew. Sustain. Energy Rev.* **51**, 1–8 (2015).
12. Zhu, W. Z. & Deevi, S. C. Development of interconnect materials for solid oxide fuel cells. *Mater. Sci. Eng. A* **348**, 227–243 (2003).
13. Zhu, W. Z. & Deevi, S. C. A review on the status of anode materials for solid oxide fuel cells. *Mater. Sci. Eng. A* **362**, 228–239 (2003).
14. Ge, X. M., Chan, S. H., Liu, Q. L. & Sun, Q. Solid oxide fuel cell anode materials for direct hydrocarbon utilization. *Adv. Energy Mater.* **2**, 1156–1181

(2012).

15. Gür, T. M. Comprehensive review of methane conversion in solid oxide fuel cells: Prospects for efficient electricity generation from natural gas. *Prog. Energy Combust. Sci.* **54**, 1–64 (2016).
16. Sauvet, A. L. & Fouletier, J. Catalytic properties of new anode materials for solid oxide fuel cells operated under methane at intermediary temperature. *J. Power Sources* **101**, 259–266 (2001).
17. Energy, G. *Modeling, Design, Construction, and Operation of Power Generators with Solid Oxide Fuel Cells*. (2018). doi:10.1007/978-3-319-75602-8
18. Bruce, M. K., van den Bossche, M. & McIntosh, S. The Influence of Current Density on the Electrocatalytic Activity of Oxide-Based Direct Hydrocarbon SOFC Anodes. *J. Electrochem. Soc.* **155**, B1202 (2008).
19. Lee, J. H. *et al.* Quantitative analysis of microstructure and its related electrical property of SOFC anode, Ni-YSZ cermet. *Solid State Ionics* **148**, 15–26 (2002).
20. Wang, Z. H. *et al.* Redox tolerance of thin and thick Ni/YSZ anodes of electrolyte-supported single-chamber solid oxide fuel cells under methane oxidation conditions. *Fuel Cells* **13**, 1109–1115 (2013).
21. Zhou, F. *et al.* Progress in Ni-based anode materials for direct hydrocarbon solid oxide fuel cells. *J. Mater. Sci.* **53**, 8747–8765 (2018).
22. Jiang, S. P. Nanoscale and nano-structured electrodes of solid oxide fuel cells by infiltration: Advances and challenges. *Int. J. Hydrogen Energy* **37**, 449–470 (2012).
23. Vernoux, P., Guillodo, M., Fouletier, J. & Hammou, A. Alternative anode material for gradual methane reforming in solid oxide fuel cells. *Solid State Ionics* **135**, 425–431 (2000).
24. Wendel, C. H., Kazempoor, P. & Braun, R. J. Novel electrical energy storage system based on reversible solid oxide cells: System design and operating conditions. *J. Power Sources* **276**, 133–144 (2015).
25. Ruiz-Morales, J. C. *et al.* LSCM-(YSZ-CGO) composites as improved symmetrical electrodes for solid oxide fuel cells. *J. Eur. Ceram. Soc.* **27**, 4223–4227 (2007).

26. Peña, M. A. & Fierro, J. L. G. Chemical structures and performance of perovskite oxides. *Chem. Rev.* **101**, 1981–2017 (2001).
27. Tanaka, H. & Misono, M. Advances in designing perovskite catalysts. *Curr. Opin. Solid State Mater. Sci.* **5**, 381–387 (2001).
28. van den Bossche, M. & McIntosh, S. The rate and selectivity of methane oxidation over La0.75Sr0.25CrxMn1-xO3-δ as a function of lattice oxygen stoichiometry under solid oxide fuel cell anode conditions. *J. Catal.* **255**, 313–323 (2008).
29. Sfeir, J. *et al.* Lanthanum chromite based catalysts for oxidation of methane directly on SOFC anodes. *J. Catal.* **202**, 229–244 (2001).
30. Tao, S. & Irvine, J. T. S. A redox-stable efficient anode for solid-oxide fuel cells. *Nat. Mater.* **2**, 320–323 (2003).
31. Zha, S., Tsang, P., Cheng, Z. & Liu, M. Electrical properties and sulfur tolerance of La0.75Sr 0.25Cr1-xMnxO3 under anodic conditions. *J. Solid State Chem.* **178**, 1844–1850 (2005).
32. Tao, S., Irvine, J. T. S. & Kilner, J. A. An efficient solid oxide fuel cell based upon single-phase perovskites. *Adv. Mater.* **17**, 1734–1737 (2005).
33. Wan, J., Zhu, J. H. & Goodenough, J. B. La0.75Sr0.25Cr0.5Mn0.5O3-δ + Cu composite anode running on H2 and CH4 fuels. *Solid State Ionics* **177**, 1211–1217 (2006).
34. Tao, S. & Irvine, J. T. S. Synthesis and Characterization of (La[sub 0.75]Sr[sub 0.25])Cr[sub 0.5]Mn[sub 0.5]O[sub 3−δ], a Redox-Stable, Efficient Perovskite Anode for SOFCs. *J. Electrochem. Soc.* **151**, A252 (2004).
35. Tao, S., Irvine, J. T. S. & Plint, S. M. Methane oxidation at redox stable fuel cell electrode la 0.75Sr0.25Cr0.5Mn0.5O 3-δ. *J. Phys. Chem. B* **110**, 21771–21776 (2006).
36. Alifanti, M., Kirchnerova, J., Delmon, B. & Klvana, D. Methane and propane combustion over lanthanum transition-metal perovskites: Role of oxygen mobility. *Appl. Catal. A Gen.* **262**, 167–176 (2004).
37. Kirchnerova, J. & Klvana, D. Design criteria for high-temperature combustion catalysts. *Catal. Letters* **67**, 175–181 (2000).
38. Royer, S., Duprez, D. & Kaliaguine, S. Role of bulk and grain boundary

oxygen mobility in the catalytic oxidation activity of LaCo1-xFexO3. *J. Catal.* **234**, 364–375 (2005).

39. Giroir-Fendler, A. *et al.* Catalytic oxidation of vinyl chloride emission over LaMnO3 and LaB0.2Mn0.8O3 (B=Co, Ni, Fe) catalysts. *Appl. Catal. B Environ.* **129**, 509–516 (2012).
40. Chanquía, C. M., Montenegro-Hernández, A., Troiani, H. E. & Caneiro, A. A bottom-up building process of nanostructured La0.75Sr 0.25Cr0.5Mn0.5O3-δ electrodes for symmetrical-solid oxide fuel cell: Synthesis, characterization and electrocatalytic testing. *J. Power Sources* **245**, 377–388 (2014).
41. Leofanti, G., Padovan, M., Tozzola, G. & Venturelli, B. Surface area and pore texture of catalysts. *Catal. Today* **41**, 207–219 (1998).
42. Cameron, K. C. & Buchan, G. D. *Porosity and Pore Size Distribution*. *Encyclopedia of Soil Science* (Published by Elsevier Inc., 2006). doi:10.1081/E-ESS-120042734
43. Storck, S., Bretinger, H. & Maier, W. F. Characterization of micro- and mesoporous solids by physisorption.pdf. *Appl. Catal.* **174**, 137–146 (1998).
44. *Impedance Spectroscopy Theory , Experiment , and Applications*. *Wiley-Interscience* (2005).
45. Aikens, D. A. *Electrochemical methods, fundamentals and applications*. *Journal of Chemical Education* **60**, (2009).
46. Jiang, S. P. & Chan, S. H. Development of Ni/Y 2 O 3 – ZrO 2 cermet anodes for solid oxide fuel cells . *Mater. Sci. Technol.* **20**, 1109–1118 (2004).
47. Kim, J. *et al.* Fabrication and characterization of all-ceramic solid oxide fuel cells based on composite oxide anode. *J. Power Sources* **241**, 440–448 (2013).
48. Thommy, L., Joubert, O., Hamon, J. & Caldes, M. T. Impregnation versus exsolution: Using metal catalysts to improve electrocatalytic properties of LSCM-based anodes operating at 600 °C. *Int. J. Hydrogen Energy* **41**, 14207–14216 (2016).
49. Jiang, S. P., Chen, X. J., Chan, S. H., Kwok, J. T. & Khor, K. A. (La0.75Sr0.25)(Cr0.5Mn0.5) O3/YSZ composite anodes for methane oxidation reaction in solid oxide fuel cells. *Solid State Ionics* **177**, 149–157 (2006).

Thanks

Per prima cosa, vorrei ringraziare la prof.ssa Antonella Glisenti. Grazie per l'opportunità che mi è stata data di poter lavorare in questo gruppo di ricerca, di avermi accompagnato in questo percorso come una guida non solo scientificamente parlando ma anche umanamente.

Grazie ai ragazzi del gruppo IMPACT, vi nomino in ordine alfabetico: Andrea, Elena, Enrico, Giacomo, Gianmaria, Giovanni e Simone. Credo che ognuno mi abbia aiutato in qualche modo a svolgere questi mesi di tesi. Anche quando ci sono stati problemi (parecchi direi) e soprattutto nell'attendere le paste d'oro e di nickel e la riparazione del forno (inerzia termica!) siete stati un'ottima compagnia, oltre che di aiuto dal punto di vista operativo. Grazie per avere creato, attraverso la pausa caffè, un gruppo in cui è facile colloquiare, non solo di cose serie.

Ringrazio la mia famiglia: mamma Stefania, papà Remigio e il mio caro batuffolo di pelo, Teddy. Grazie per la pazienza portata e per l'opportunità di conseguire gli studi sino ad ora. Ogni risultato è senza dubbio dedicato a voi.

Infine, ringrazio Valter e Diana per la disponibilità e gentilezza nei miei confronti.

Per ultimo ma non meno importante ringrazio Diego. Senza la tua pazienza, perché ogni tanto ce ne hai, non sarei riuscita ad andare avanti quando vedevo tutto nero cosa che accade parecchio spesso. Grazie per essere il mio primo sostenitore e per avere la capacità di tirarmi su di morale anche quando credo di non potercela fare.